



Spring photosynthetic onset and net CO₂ uptake in Alaska triggered by landscape thawing

Nicholas C. Parazoo¹  | Almut Arneth² | Thomas A. M. Pugh^{3,4} | Ben Smith⁵ | Nicholas Steiner⁶ | Kristina Luus⁷ | Roisin Commane⁸ | Josh Benmergui⁸ | Eric Stofferahn⁹ | Junjie Liu¹ | Christian Rödenbeck¹⁰ | Randy Kawa¹¹ | Eugenie Euskirchen¹² | Donatella Zona¹³  | Kyle Arndt¹³ | Walt Oechel¹³ | Charles Miller¹

¹California Institute of Technology, Jet Propulsion Laboratory, Pasadena, California

²Institute of Meteorology and Climate Research (IMK-IFU), Karlsruhe Institute of Technology, Garmisch-Partenkirchen, Germany

³School of Geography, Earth and Environmental Sciences, University of Birmingham, Birmingham, UK

⁴Birmingham Institute of Forest Research, University of Birmingham, Birmingham, UK

⁵Department of Physical Geography and Ecosystem Science, Lund University, Lund, Sweden

⁶Department of Earth and Atmospheric Sciences, The City College of New York, New York, New York

⁷Centre for Applied Data Analytics, Dublin, Ireland

⁸Department of Earth and Planetary Sciences, Harvard University, Cambridge, Massachusetts

⁹Conservation Science Partners, Truckee, California

¹⁰Max Planck Institute for Biogeochemistry, Jena, Germany

¹¹NASA Goddard Space Flight Center, Greenbelt, Maryland

¹²Institute of Arctic Biology, University of Alaska Fairbanks, Fairbanks, Alaska

¹³Biology Department, San Diego State University, San Diego, California

Correspondence

Nicholas C. Parazoo, California Institute of Technology, Jet Propulsion Laboratory, Pasadena, CA.

Email: nicholas.c.parazoo@jpl.nasa.gov

Funding information

National Science Foundation Arctic Observation Network program, Grant/Award Number: 1503912; boreal flux towers; National Science Foundation (NSF), Grant/Award Number: 1702797; National Aeronautics and Space Administration, Grant/Award Number: NNX15AT74A, NNX16AF94A; ABoVE; European Union's Horizon 2020 research, Grant/Award Number: 727890

Abstract

The springtime transition to regional-scale onset of photosynthesis and net ecosystem carbon uptake in boreal and tundra ecosystems are linked to the soil freeze–thaw state. We present evidence from diagnostic and inversion models constrained by satellite fluorescence and airborne CO₂ from 2012 to 2014 indicating the timing and magnitude of spring carbon uptake in Alaska correlates with landscape thaw and ecoregion. Landscape thaw in boreal forests typically occurs in late April (DOY 111 ± 7) with a 29 ± 6 day lag until photosynthetic onset. North Slope tundra thaws 3 weeks later (DOY 133 ± 5) but experiences only a 20 ± 5 day lag until photosynthetic onset. These time lag differences reflect efficient cold season adaptation in tundra shrub and the longer dehardening period for boreal evergreens. Despite the short transition from thaw to photosynthetic onset in tundra, synchrony of tundra respiration with snow melt and landscape thaw delays the transition from net carbon loss (at photosynthetic onset) to net uptake by 13 ± 7 days, thus reducing the tundra net carbon uptake period. Two global CO₂ inversions using a CASA-GFED model prior estimate earlier northern high latitude net carbon uptake compared to our regional inversion, which we attribute to (i) early photosynthetic-onset

model prior bias, (ii) inverse method (scaling factor + optimization window), and (iii) sparsity of available Alaskan CO₂ observations. Another global inversion with zero prior estimates the same timing for net carbon uptake as the regional model but smaller seasonal amplitude. The analysis of Alaskan eddy covariance observations confirms regional scale findings for tundra, but indicates that photosynthesis and net carbon uptake occur up to 1 month earlier in evergreens than captured by models or CO₂ inversions, with better correlation to above-freezing air temperature than date of primary thaw. Further collection and analysis of boreal evergreen species over multiple years and at additional subarctic flux towers are critically needed.

KEYWORDS

boreal, carbon cycle, eddy covariance, freeze–thaw, inversion, remote sensing, tundra, vegetation fluorescence

1 | INTRODUCTION

The future trajectory of the Arctic–Boreal Zone as a net carbon (C) sink or source is of global importance due to vast quantities of C stored in permafrost (Hugelius et al., 2014). Climate warming threatens to thaw and release permafrost C back to the atmosphere as the greenhouse gases, carbon dioxide (CO₂) and methane, creating a positive feedback and promoting further global warming (Hinzman et al., 2013). At the same time, warming can lead to higher productivity (Natali, Schuur, & Rubin, 2012), creating temporary C sinks via increased above-ground biomass and delayed decomposition, and offsetting potential C losses. The remainder of this paper focuses on C in the form of CO₂.

The balance of net ecosystem C gain and loss processes is strongly modulated by land surface freeze–thaw dynamics, the timing and duration of seasonal soil thawing (defined as the transition from frozen to unfrozen soil water state), vegetation growing season, and surface moisture supply (Kim et al., 2014; Yi, Wischniewski, Langer, Muster, & Boike, 2014). In spring, plant productivity (denoted as gross primary production or GPP) is hindered by cold temperatures and lack of liquid water in frozen soils and snow cover. Climate warming promotes earlier landscape thawing (Goulden, 1998), reduced spring snow cover duration (Lawrence & Slater, 2010), earlier budburst (Badeck et al., 2004), and longer growing seasons (Barichivich et al., 2013). These processes lead to higher GPP through simultaneous warming, CO₂ fertilization, and increased woody biomass (Bhatt et al., 2010; Elmendorf et al., 2012; McGuire et al., 2012). Earlier spring snow melt and thawing also expose the land surface to increasing solar absorption resulting in a longer decomposition season, active layer deepening, extended zero curtain period, and talik formation, which can stimulate terrestrial ecosystem respiration (TER) through enhanced soil warming and water drainage (Lawrence, Slater, Romanovsky, & Nicolsky, 2008; Romanovsky & Osterkamp, 2000).

The impacts of changes in growing season length on annual C balance are not well modeled (Schaefer et al., 2012). In particular,

earth system models used in IPCC climate assessments predict photosynthetic-growing season onsets that are systematically early on local (Peng et al., 2015) to regional scales (Commane, Lindaas et al., 2017). In turn, GPP biases propagate through the model and affect the timing and magnitude of estimated net biosphere production (NBP; Wang et al., 2012), representing the balance of GPP and TER (NBP = GPP–TER). As climate change at high latitudes promotes earlier and longer growing seasons (Barichivich et al., 2013; Kim, Kimball, Zhang, & McDonald, 2012), while the photoperiod remains fixed, models with early spring bias in the current climate are likely to underestimate the photosynthetic response to future warming. Consequently, errors in the simulation of growing season onset and duration provide a plausible explanation for the tendency of earth system models to underestimate peak-growing season C uptake in response to climate warming (Graven et al., 2013).

It is well known that changes in spring GPP onset in cold northern latitudes corresponds closely with changes in the date of soil thaw when liquid water becomes available (Black et al., 2000; Goulden, 1998; Jarvis & Linder, 2000; Troeng and Linder, 1982). In evergreen needleleaf forests (denoted evergreens), assimilated C initially accumulates as starch following soil thaw and then is used to grow new foliage, branches, and stem during the growing season peak (Bergh, McMurtrie, & Linder, 1998). GPP onset can occur several weeks prior to changes in biomass in conifers (Ottander, Campbell, & Oquist, 1995; Richardson, Braswell, Hollinger, Jenkins, & Ollinger, 2011; Soukupova et al., 2008), but the spring-dehardening period, during which plants undergo the biochemical changes needed for green-up, can slow recovery from winter dormancy (Ensminger, Schmidt, & Lloyd, 2008). Land surface models that do not account for effects of frozen soils or recovery of photosynthetic capacity in spring and summer overestimate GPP gain by up to 10% across the entire permafrost domain (Jafarov & Schaefer, 2016) and up to 40% in boreal forests (Bergh et al., 1998). However, the relationship between spring GPP onset and soil freeze–thaw is complicated by confounding air temperature and snow cover effects, which can lead to GPP onset

while soils are frozen (Arneth, Lloyd, Shibistova, Sogachev, & Kolle, 2006; Ensminger et al., 2004; Gonsamo, Chen, Price, Kurz, & Wu, 2012; Jonsson, Eklundh, Hellström, Bähring, & Jönsson, 2010; Pulliainen et al., 2017; Walther et al., 2016).

Tundra ecosystems in the far northern Alaskan and Siberian Arctic also show a pattern of increased GPP and NBP in spring with warming and earlier soil thaw and snow melt (Arneth et al., 2006; Griffis, Rouse, & Waddington, 2000; Harazono, Mano, Miyata, Zulueta, & Oechel, 2003; Lafleur & Humphreys, 2007; Ueyama et al., 2013). The length of time from soil thaw to onset of GPP and net C uptake (date when ecosystem shifts from net C source to net sink), however, varies under different environmental conditions and vegetation types. Simultaneous increases in soil respiration (i.e., TER) with GPP following thaw and snow melt can delay daily net C uptake by 5–23 days depending on ambient temperature (Lafleur & Humphreys, 2007; Oberbauer, Starr, & Pop, 1998). Ecosystem type and fraction of evergreen vs. deciduous species are also important. Multiyear observations from a cluster of flux towers on the Alaskan North Slope show much stronger correlation of thaw date with heath- and wet-sedge tundra than with tussock tundra (Euskirchen, Bret-Harte, Shaver, Edgar, & Romanovsky, 2017). Likewise, evergreen mosses and lichens transition to net uptake within 1 week of snow melt, while deciduous shrubs transition more slowly over 1–3 weeks (Lafleur & Humphreys, 2007). Direct observations of *Sphagnum* (moss) along the northern coast of Alaska, near Barrow, show very weak levels of initial photosynthesis following snow melt due to photoinhibition as a stress response to high radiation levels, causing a delay in net C uptake of ~3 weeks (Zona et al., 2011). The exact timing of spring GPP onset and transition to net C uptake in Arctic tundra and in boreal ecosystems is, thus, not well established at regional scale, in part due to sparse and variable results from field measurements, and also because reliable indicators of GPP onset are limited.

Solar-induced chlorophyll fluorescence (SIF) measures a direct outcome of foliar light absorption by chlorophyll and provides an important seasonal GPP proxy (Frankenberg et al., 2011; Parazoo et al., 2014). Recent satellite SIF measurements have been used to accurately represent the timing of spring GPP onset and the duration of growing season C uptake in Alaskan ecosystems (Commane, Lindaas et al., 2017; Jeong et al., 2017; Luus et al., 2017; Walther et al., 2016). In particular, Luus et al. (2017) show green-up and budburst to occur 1–2 weeks prior to SIF-based GPP onset in northern high latitude deciduous tundra ecosystems. Moreover, leaf-level SIF measurements show close correspondence to photochemical reflectance index and chlorophyll carotenoid index optical indices during spring photosynthetic activation (from gas exchange measurements) in boreal evergreens, reflecting a reversal of non-photochemical quenching and leaf pigments in spring with changes in chloroplast functioning during cold dehardening (Springer, Wang, & Gamon, 2017; Wong & Gamon, 2015). Especially in evergreens, SIF remote sensing has potential to provide a powerful measure of the reactivation of photosynthesis in spring at large spatial scales,

which is otherwise invisible and difficult to assess with reflectance-based optical indices (Walther et al., 2016; Wong & Gamon, 2015).

The analysis of SIF–GPP relationships in Alaska has shed light on the effects of plant structural vs. functional phenology changes on seasonal C fluxes across key Arctic biomes and helped quantify Alaskan C balance (Commane, Lindaas et al., 2017), but have not yet clarified links between plant phenology and environmental effects in driving seasonal onset of GPP and net C uptake. As such, our quantitative and mechanistic understanding of links between environmental forcing, phenology response, and plant C uptake across tundra and boreal ecosystems requires further refining and improved estimates of the timing of thaw, GPP, and net C uptake at regional scale. Here, we establish empirical relationships between spring thaw, GPP onset, and net C uptake at regional scale as derived from established GPP and NBP estimates constrained by satellite fluorescence and airborne CO₂ observations in Alaska (Luus et al., 2017; Commane, Lindaas et al., 2017). We also analyze regional estimates against eddy covariance observations at boreal and tundra tower sites in interior and North Slope Alaska. By quantifying these relationships, we seek to determine the extent to which landscape thaw controls the timing of GPP and net C uptake onset in northern ecosystems and understand the ecosystem dependencies and physiological mechanism behind the timing and time lag of thaw and C fluxes.

2 | MATERIALS AND METHODS

2.1 | Freeze–thaw state determination

Daily 10-km resolution maps of the bulk freeze–thaw state of the Alaskan land surface were determined for 2012–2014 using passive microwave observations from the Advanced Microwave Scanning Radiometer-EOS (AMSR-E) and the Special Sensor Microwave Imager/Sounder (SSMIS-F17). The freeze–thaw mapping algorithm is based on wavelet analysis, which uses a time series singularity classifier to identify the timing of freeze–thaw and snow melt transitions (Steiner, McDonald, Dinardo, & Miller, 2015; Steiner, McDonald, & Miller, 2017a,b; Steiner & Tedesco, 2014). A brightness temperature gradient ($K-K_0$ Bands), sensitive to transitions between frozen and liquid state of water caused by contrasts in the bulk landscape complex dielectric constant, is used to determine freeze–thaw status (Zhang, Kimball, Kim, & McDonald, 2011). Peak diurnal difference brightness temperatures determine snow melt status (Ramage & Isacks, 2002). Here, freeze–thaw state represents the transition of bulk Alaskan landscapes from frozen to unfrozen conditions and does not distinguish between landscape components (soil, vegetation, and snow).

2.2 | Regional GPP and NBP flux estimates

Regional GPP is taken from the Polar Vegetation Photosynthesis and Respiration Model (PVPRM; Luus & Lin, 2015). PVPRM is a functional representation of ecosystem C fluxes parameterized using eddy covariance data for seven arctic and boreal vegetation types; it

is applied regionally and temporally using prescribed satellite phenology and North American Regional Reanalysis (NARR) meteorology to obtain three hourly GPP, TER, and NBP at $1/6^\circ$ latitude \times $1/4^\circ$ longitude in Alaska. Phenology is driven by monthly SIF from the Global Ozone Monitoring Experiment-2 (GOME-2) satellite (Joiner, Yoshida, Vasilkov, Schaefer, & Jung, 2014; Luus et al., 2017). GOME-2 SIF at 740 nm is derived using a statistically based retrieval, which optimizes model parameters for atmospheric absorption, surface reflectance, and fluorescence radiance using empirical principal component analysis, to enhance retrieval precision and reduce noise. Cloud screening is applied such that only pixels with cloud fraction $<40\%$ are retained, removing primarily heavily clouded (overcast) pixels within the 40×80 km GOME-2 footprint. The main effect of the remaining clouds is a shielding effect, which masks a fraction of the observed scene (80% of surface observed for 40% cloud cover and cloud optical thickness up to 10) but does not alter the spectral signature of fluorescence (Joiner et al., 2012; Joiner et al., 2014). To alleviate reduced signal-to-noise soundings for low sun angles over snow and other high albedo surfaces in northern high-latitude spring, GOME-2 SIF values are additionally screened for solar zenith angles less than 60° and cloud fractions below 20%, aggregated monthly and separately calculated for each vegetation class, then weighted according to component vegetation fractions at each PVPRM pixel (Luus et al., 2017). We refer to SIF-driven GPP as PVPRM-SIF GPP. We also compare monthly constrained PVPRM-SIF GPP to 5-day mean SIF (same screening criteria) to assess the impact of monthly aggregation on seasonal transitions.

PVPRM NBP in Alaska is further optimized using atmospheric CO_2 vertical profiles obtained in the lower atmosphere across Alaska during the Carbon in the Arctic Reservoirs Vulnerability Experiment (CARVE; Chang et al., 2014; Commane, Lindaas et al., 2017). Profiles were acquired from April to November during CARVE campaigns from 2012 to 2014 and converted to mass-weighted, column-mean CO_2 mole fraction in the atmospheric residual layer. The NBP optimization approach uses the CARVE Polar Weather Research and Forecasting—Stochastic Time-Inverted Lagrangian Transport (PWRFS-TILT) framework (Henderson et al., 2015) to calculate the influence function of land surface fluxes on CARVE profiles. Modeled partial column CO_2 enhancements are obtained by convolving the land surface influence functions with NBP priors from PVPRM, which were aggregated to $0.5^\circ \times 0.5^\circ$ for the CO_2 inversion. For each 2-week measurement period, additive corrections are made to PVPRM NBP that minimized the differences between modeled and observed column CO_2 enhancements, providing spatially explicit, data-constrained NBP for Alaska for each interval. Initial and final campaign dates varied each year, starting and ending on May 27, 2012 and September 26, 2012, April 2, 2013 and October 26, 2013, and May 23, 2014 and November 9, 2014, with mean start and end dates on day of year (DOY) 127 and 293. We consider optimized NBP as most valid between mid-May and mid-October, although we note that CO_2 fluxes in January–March compare well to near surface CO_2 observations at CRV and BRW towers as determined from STILT footprints (Commane, Lindaas et al., 2017). Additive flux corrections are linearly

interpolated between aircraft measurement periods and use PVPRM prior flux for late winter when CARVE flights are not available (December–March) to obtain regional NBP for Alaska (daily, $0.5^\circ \times 0.5^\circ$). CARVE NBP estimates are denoted as CARVE-Opt (Commane, Benmergui et al., 2017; <https://doi.org/10.3334/ornl-daac/1389>).

Commane, Lindaas et al. (2017) account for uncertainties in observations, background, transport, and the model prior in CARVE-Opt using restricted maximum likelihood estimation and then generate 10,000 realizations of the additive flux correction. The standard deviation produces regionally aggregated errors of $-0.25 \text{ gC m}^{-2} \text{ day}^{-1}$ in spring and $0.50 \text{ gC m}^{-2} \text{ day}^{-1}$ in summer, which translates to a net C uptake onset error of 5–10 days on average (cf figure 3, Luus et al., 2017 and figure 1, Commane, Lindaas et al., 2017). We do not explicitly account for these uncertainties in our analysis but consider this timing error in our qualitative analysis of Alaskan net C uptake onset.

We provide an indirectly optimized estimate of TER as the difference between PVPRM-SIF GPP and CARVE-Opt NBP, replacing the unconstrained estimate provided by PVPRM. Given that PVPRM-SIF and CARVE-Opt are directly constrained by observations, we consider TER the more uncertain term in this analysis. Since NBP is a small number that balances larger GPP and TER components, small errors in NBP and GPP could lead to large-compensating errors in TER. To reduce these compensating errors, we apply a constraint on the signs of TER and GPP to ensure that the estimated TER is physically realistic (Bloom & Williams, 2015), and estimate TER as

$$\text{TER} = \text{NBP} \times a + \text{GPP} \times b$$

where a and b reflect a range of possible scale factors based on estimated NBP and GPP normally distributed uncertainties of 50% (1-sigma range of 0.5–1.5 for a and b). We then sample 1000 samples of TER vectors and reject unphysical values ($\text{TER} < 0$).

We analyze CARVE-Opt NBP against an ensemble of three global inverse estimates constrained against satellite or surface CO_2 observations: (i) NASA Carbon Monitoring System Flux (CMS-Flux) estimation and attribution strategy (Liu et al., 2014, 2017; Ott et al., 2015) constrained by column CO_2 from the Greenhouse gases Observing SATellite (GOSAT) using the v7.3 ACOS retrieval algorithm; (ii) CarbonTracker 2016 (CT2016) (Peters et al., 2007, with updates documented at <http://carbontracker.noaa.gov>) constrained by 124 datasets from a global network of tower, aircraft, and ship-board surface in situ CO_2 observations; and (iii) Jena CarboScope s04_v4.1 (Jena4.1) (update of Rödenbeck, Houweling, Gloor, & Heimann, 2003; Rödenbeck, 2005) constrained by surface observations at 59 sites. All inverse estimates have been analyzed for the period 2012–2014.

We also analyze simulated GPP and NBP from the CASA-GFED3 model (Van der Werf et al., 2010), which is run at $0.5^\circ \times 0.5^\circ$ monthly resolution and scaled to 3 hr and $1^\circ \times 1.25^\circ$ for CO_2 -modeling studies (<https://nacp-files.nacarbon.org/nacp-kawa-01/>). Biomass burning and fuel wood C emissions were estimated by the model on daily and monthly time step. These calculations are driven

by analyzed meteorological data (MERRA) from the Goddard Modeling and Assimilation Office from 2003 to 2016.

2.3 | Flux tower site description

Data for this study were collected from eight eddy covariance towers across four sites on the North Slope and in Interior Alaska (Figure 1). Brief site descriptions, including location, years analyzed, and references, are provided in Table 1. Tundra sites consist of five total towers at three sites in the North Slope of Alaska, including one tower each at Atqasuk (ATQ) and Ivtokuk (IVO) and three towers at Imnavait Creek Watershed (IMN). Boreal sites include three towers at the Bonanza Creek Experimental Forest (BON) in Interior Alaska. NBP measurements were collected at each of the eight eddy covariance towers for at least 1 year during 2012–2014 and partitioned into GPP and TER components using the relation between NBP during the nighttime ($PAR < 50 \mu\text{mol m}^{-2} \text{s}^{-1}$) and air temperature (Euskirchen et al., 2017; Reichstein et al., 2005). An additional technique using daytime light partitioning at ATQ and IVO (Lasslop et al., 2010) is analyzed for comparison. All NBP and GPP estimates are processed as half hourly means, then gap filled and averaged daily. The data-processing methodologies for BON and IMN are described in Euskirchen, Edgar, Turetsky, Waldrop, and Harden (2014) and Euskirchen et al. (2017), respectively, and for ATQ and IVO in Goodrich et al. (2016). For each location, we sample PVPRM-SIF GPP and CARVE-Opt NBP only for years with available eddy covariance data from 2012 to 2014 (see Table 1).

BON is our most southerly site, consisting of three stations in the boreal peatland lowlands of the Tanana Flats of interior Alaska within 0.5 km of each other (Euskirchen et al., 2014). These sites are ~30 km southeast of Fairbanks and vary in the presence and stability of permafrost. They include a black spruce ecosystem with cold soils and permafrost (BON-Spr), a collapse scar bog representing recent permafrost thaw (BON-Bog) and a rich fen-lacking permafrost (BON-Fen). BON-Spr is dominated by mature black spruce trees (*Picea mariana*, ~100 years old), with an understory consisting of shrubs, mosses, grasses, and lichens, and sits on an intact peat plateau that rises ~130 cm from the surrounding landscape. BON-Bog is a circular depression that formed through thermokarst and contains active thaw margins with a significant dieback of *Picea mariana*. BON-Fen is composed of grasses, sedges, and forbs. The sites are in proximity (<0.5 km) and thus collocated within a single grid box of CARVE-Opt and PVPRM-SIF.

IMN is located in the northern foothills of the Brooks Range in northern Alaska (Euskirchen et al., 2017). The watershed is underlain by continuous permafrost, with predominant soils containing 15–20 cm of organic peat underlain by silt and glacial till. The mean annual air temperature (MAT) from 1988 to 2007 was -7.4°C and the mean annual precipitation was 318 mm, with about 40% occurring as rain and 60% as snow. The landscape is treeless, located approximately 100 km north from latitudinal treeline. IMN includes three stations across three unique tundra sites, including heath (IMN-Hth), moist acidic tussock (IMN-Tus), and wet sedge (IMN-

Sed). These sites are also in proximity (<0.5 km) and therefore share the same grid box.

IVO is located ~300 km to the south of the Arctic Ocean at the foothills of the Brooks Range, with a MAT and summer precipitation of -8.9°C and 210 mm from 2003 to 2008. IVO vegetation is dominated by tussock-sedge, dwarf-shrub, and moss tundra, and represents the dominant vegetation type in Alaska (Zona et al., 2016). Tussock tundra on flat ground consists of 57% *E. vaginatum* tussocks, 42% intertussock vegetation (dominated by *Sphagnum* moss), and 1% moss-dominated hollows (Davidson et al., 2016). The most northerly site, ATQ, is ~100 km south of the Arctic Ocean. MAT and summer precipitation in ATQ have been -10.8°C and 100 mm, respectively, for the 1999–2006 period. ATQ vegetation is dominated by tundra sedges, grasses, mosses, and some dwarf shrubs <40 cm tall. Tussock tundra on dry ridges and plateaus comprised 21% *Eriophorum vaginatum* tussocks and 79% intertussock areas, which are dominated by moss and evergreen dwarf shrubs (Davidson et al., 2016). ATQ has land cover typical of arctic wetlands (Zona et al., 2016).

2.4 | Analysis

We analyze the period 2012–2014 in Alaska (58°N – 72°N , 140°W – 170°W) due to the availability of CARVE-Opt data. All regional freeze-thaw, GPP, and NBP datasets are aggregated to $0.5^{\circ} \times 0.5^{\circ}$ and then averaged across years to provide a 3-year climatology. This

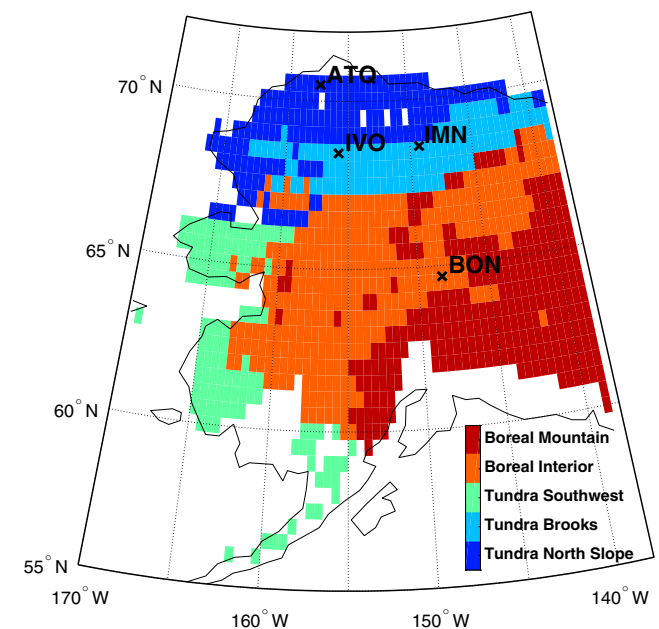


FIGURE 1 Map showing spatial pattern of vegetation and location of flux towers. Vegetation is derived from US EPA Level 2 ecoregion maps for boreal (reds) and tundra (blue). Tower sites include Bonanza Creek (BNZ: 64.70°N , 148.32°W), Imnavait (IMN: 68.62°N , 149.30°W), Ivtokuk (IVO: 68.48°N , 155.75°W), and Atqasuk (ATQ: 70.47°N , 157.40°W). IMN and BON sites each include three additional eddy covariance stations (see Table 1)

TABLE 1 Site characteristics of eddy covariance flux towers for Alaska

Site name/ID	Ecosystem/station ID	Region	Latitude, longitude	Elevation	Site years analyzed	References
Bonanza Creek Experimental Forest (BON)	Black Spruce Forest (BON-Spr)	Interior Alaska	64.696°N, 148.323°W	100 m	2012–2013	Euskirchen et al. (2014)
	Thermokarst collapse scar bog (BON-Bog)	Interior Alaska	64.695°N, 148.321°W	100 m	2012–2013	Euskirchen et al. (2014)
	Rich fen (BON-Fen)	Interior Alaska	64.703°N, 148.313°W	100 m	2012–2013	Euskirchen et al. (2014)
Imnavait Creek Watershed (IMN)	Wet sedge tundra (IMN-Sed)	North Slope Alaska	68.606°N, 149.311°W	920 m	2012–2014	Euskirchen et al. (2017)
	Moist acidic tussock tundra (IMN-Tus)	North Slope Alaska	68.606°N, 149.304°W	930 m	2012–2014	Euskirchen et al. (2017)
	Heath tundra (IMN-Hth)	North Slope Alaska	68.607°N, 149.296°W	940 m	2012–2014	Euskirchen et al. (2017)
Ivotuk (IVO)	Tundra dominated by tussock-sedge, dwarf-shrub, moss	North Slope Alaska	68.486°N, 155.750°W	543 m	2014	Goodrich et al. (2016) and Zona et al. (2016)
Atqasuk (ATQ)	Tundra dominated by sedge, grass, dwarf shrub	North Slope Alaska	70.469°N, 157.409°W	24 m	2014	Goodrich et al. (2016) and Zona et al. (2016)

study focuses on climatological spatial patterns over this period, rather than year-specific patterns or interannual variability, to provide a first assessment of thaw-C uptake patterns over Alaska. We define seasonal-onset dates for snow melt, thaw, GPP, and net C uptake for each grid point in the climatological mean. We acknowledge our short 3-year period provides a small sample of northern high-latitude springs but captures a range of variability including an average spring in 2012, cool and late spring in 2013, and warm and early spring in 2014 (Commane, Lindaas et al., 2017; Cox et al., 2017; Davidson et al., 2016; Euskirchen et al., 2014).

Primary spring thaw is defined as the first DOY when a 14-day running filter contains at least 13 days when the land surface was classified as thawed. This high threshold (13 of 14 days, or 93%) discriminates against early “false thaws” and extended diurnal thaw–refreeze cycles that characterize the Alaskan spring. Previous work (Kim et al., 2012) demonstrates that even an 80% threshold is insufficiently stringent and defines a growing season start date that is too early. Snow melt date is identified as a one-time switch indicating wet snow with sensitivity to melt–refreeze cycles minimized. We analyze freeze–thaw date as the primary switch for GPP onset, but provide a brief analysis of snow melt to provide context for spring respiration. We define the GPP-onset date as the mean DOY when GPP is between 10% and 20% of GPP_{max} for that year, accounting for observation noise and range of transition dates from slow to rapid spring recovery in tundra and boreal ecosystems. We define the net C uptake start as the first DOY when $NBP > 0 \text{ gC m}^{-2} \text{ day}^{-1}$.

We analyze only grid points with average elevation $<1,300 \text{ m}$ (no alpine vegetation) and <60 days of reported thaw or snow melt status from January 1 to spring thaw date as identified above. This filter isolates data with smooth seasonal transition between frozen and thawed conditions and clearly demarcated frozen winter soils from thawed summer soils. Results are analyzed separately for

individual land cover types from Environmental Protection Agency Level 2 and 3 North America ecoregion maps (Figure 1; <https://www.epa.gov/eco-research/ecoregions>), with high-elevation pixels masked out in white. The primary land cover types analyzed are tundra and boreal, which are subdivided into the following geographical subregions: Tundra Southwest (includes Seward Peninsula, Subarctic Coastal Plains, and Bristol Bay–Nushagak Lowlands), Tundra North Slope (Arctic Coastal Plain and Arctic Foothills), Tundra Brooks (includes Brooks Range), Boreal Interior in central Alaska (Interior Forested Lowlands, Uplands, and Bottomlands), and Boreal Mountains in southeast Alaska (Interior Highlands and Ogilvie Mountains).

3 | RESULTS

3.1 | Flux tower evaluation

Observationally constrained estimates of seasonal GPP and NBP (PVPRM-SIF and CARVE-Opt, respectively) are sampled at and compared to eddy covariance towers (for years with available eddy covariance data, Table 1) for individual sites in Figures S1 and S2, using native-optimized grids (PVPRM-SIF: $1/6^\circ \times 1/4^\circ$; CARVE-Opt: $0.5^\circ \times 0.5^\circ$). PVPRM-SIF and eddy covariance GPP show high consistency of seasonal amplitude, including decreasing amplitude moving north from southern boreal (BON) to northern tundra (IMN, IVO). The high spatial resolution of PVPRM-SIF resolves spatial gradients across diverse landscapes including low GPP (relative to surrounding pixels) at BON and relatively high GPP at IMN (Figure S3). PVPRM-SIF overestimates growing season GPP at the northern most site (ATQ, Figure S1H) by a factor of 2–3 depending on partitioning technique (larger error using daytime partitioning at IVO and ATQ). We note a possible calibration bias at ATQ linked to PVPRM model parameter calibration against 2005 ATQ data (Luus & Lin, 2015; evidence supporting this claim provided in Discussion). We find

consistency in the seasonal phase, including timing of GPP onset, at all tundra sites (IMN, IVO, and ATQ), but delayed GPP onset in the lowland boreal landscapes at the BON towers (Figure S1A–C). At the BON towers and especially BON-Spr, eddy covariance GPP onset occurs ~1 month earlier than estimated by PVPRM-SIF or implied by GOME-2 SIF retrievals sampled at each site.

CARVE-Opt NBP is less consistent with eddy covariance data (Figure S2). Seasonal amplitude is overestimated at BON boreal sites, underestimated at IMN and IVO tundra sites, and overestimated at ATQ tundra. Reduced agreement of CARVE-Opt NBP (relative to GPP) is attributed to spatial aggregation errors, due to regridding of PVPRM NBP from its native grid ($1/6^\circ \times 1/4^\circ$) to the coarser $0.5^\circ \times 0.5^\circ$ grid used as the CARVE-Opt prior. The effect is seen clearly in maps of PVPRM NBP at native and aggregated resolutions (Figures S4 and S5, respectively). Finer scale structure is ultimately smoothed out in CARVE-Opt NBP (Figure S6). As such, sampling NBP at the native resolution produces higher agreement with tower data than prior and optimized NBP at coarser resolution (Figure S2).

Across-site averages of GPP and NBP for combined tundra (IMN, IVO, ATQ) and boreal (BON) sites are shown in Figure 2. Here, PVPRM-SIF GPP and CARVE-Opt NBP are sampled at the eddy covariance tower. Spatial averaging improves the NBP comparison at all sites, but especially at IVO and IMN, which exhibit strong gradients of increasing NBP to the south. Estimates of the onset date for GPP and net C uptake are within range of eddy covariance observations at tundra sites, but 1-month late at BON. Tundra GPP onset is identical (DOY 155), while CARVE-Opt net C uptake is only 6 days late (DOY 170 vs. 164) despite a larger net C source through late spring. Boreal GPP onset is 32 days later (DOY 136 vs. 104) and net C uptake 25 days later (DOY 153 vs. 128). GOME2-SIF shows earlier recovery than PVPRM-SIF, but the initial onset is still later than in eddy covariance data. Thaw onset (from AMSR-E and SSMIS-F17) occurs on average on DOY 102 at BON and DOY 130 at tundra sites.

Overall, flux towers and observationally constrained estimates show consistent patterns of C flux onset when averaged across boreal and tundra locations. This includes earlier onset of GPP and net C uptake at our boreal location and lag times of ~4 weeks between thaw and GPP onset at tundra locations. We also find consistent time lags between onset of GPP and net C uptake, with shorter lags in tundra (15 vs. 9 days for observationally constrained and eddy covariance estimates, respectively) and longer lags for boreal (17 vs. 24 days).

Focusing on the relative time lag between thaw and GPP onset shows very different patterns in boreal vs. tundra; PVPRM-SIF shows similar time lags in boreal and tundra locations (~33 days), whereas flux towers show no lag in boreal forests but a 33-day lag in tundra. These discrepancies are attributed primarily to late GPP-onset bias in PVPRM-SIF in boreal forests, which is linked in part to late morning GOME-2 SIF snapshots and thus unresolved diurnal photosynthetic signals in evergreens (e.g., Figure S7). We elaborate on these discrepancies in the Discussion. Regional patterns of thaw and onset of GPP and net C uptake are examined in more detail below.

3.2 | Regional analysis

In contrast to eddy covariance data, regional analysis indicates a systematic pattern of reduced time until GPP onset for later thaw dates. Figure 3a–c shows spatial gradients of spring-onset dates for thaw, GPP, and net C uptake. Mean-onset dates for boreal and tundra regions are summarized in Table 2. The spatial pattern is characterized by early thaw, GPP onset, and net C uptake in boreal forests (DOY 111 ± 7 , 141 ± 5 , 145 ± 10 days in the 2012–2014 average, respectively), and delayed onset in tundra (DOY 127 ± 10 , 151 ± 5 , 163 ± 10 days, respectively), consistent with warmer southern boreal climate and cooler northern tundra climate. Uncertainty is estimated here as sample uncertainties (*SD*), with random errors in CARVE-Opt (~5 days) added to net C uptake date using sum of errors. Subregional variability is negligible in boreal forests, which is clumped in the interior and southeast, and strongly latitude dependent in tundra ecosystems from southwest to northern Alaska. In tundra, thaw (DOY 119 ± 15 , 126 ± 5 , 133 ± 5), GPP onset (DOY 146 ± 6 , 150 ± 3 , 153 ± 3), and net C uptake (DOY 159 ± 11 , 161 ± 8 , 168 ± 9) become later moving north from Tundra Southwest, Brooks, and North Slope subregions.

While thaw and GPP-onset dates are later in tundra compared to boreal regions, the lag time between thaw and GPP onset (Figure 3d) decreases slightly across the same regions. Lag times range from 40 days in the southern mountains (Alaska Range and Alaska Peninsula Mountains) to ~10 days along the west and north coast (Seward Peninsula and Arctic Coastal Plain) and correspond to average lag times of 29 ± 6 days in boreal regions and 23 ± 7 days in tundra. We also find a high correlation between thaw and GPP onset ($R^2 = .69$; p -value $< .001$) with slope less than one ($\text{DOY}_{\text{thaw}} = 0.5 \times \text{DOY}_{\text{GPP}} + 79.5$, where DOY_{thaw} and DOY_{GPP} denote dates of thaw and GPP onset) and consistency across ecoregions (Figure 4a). Seasonal change in incident shortwave radiation (derived from NCEP2 downwelling shortwave), which increases later in spring moving north, is consistent with the spatial pattern of GPP onset, but shows weaker grid scale correlation with GPP onset compared to thaw onset. We test this by regressing GPP onset against two shortwave onset metrics: (i) shortwave at the time of thaw onset, and (ii) onset date of shortwave (10%–20% of its annual peak). This analysis yields $R^2 = .30$ and $.31$, respectively, representing weak correlations compared to thaw onset ($R^2 = .69$). Furthermore, high latitude tundra receives higher radiation levels at thaw onset than forests to the south; on average, incident radiation along the North Slope exceeds Boreal Interior values by 20% (290 ± 25 vs. $241 \pm 26/\text{Wm}^2$) due to later tundra thaw onset (DOY = 133 vs. 110). The convergence of soil thawing and seasonal phenology with latitude suggests that tundra ecosystems are well adapted to take advantage of this extra light within 2–4 weeks of thaw onset (more detail on physiological mechanisms in Discussion).

The magnitude of spring GPP and NBP also decreases with later thaw date, but their relationship to each other is ecosystem dependent (Figure 4b–d). We analyze GPP sensitivity during the 1-month period from May 15 to June 15, following earliest ecosystem mean GPP onset

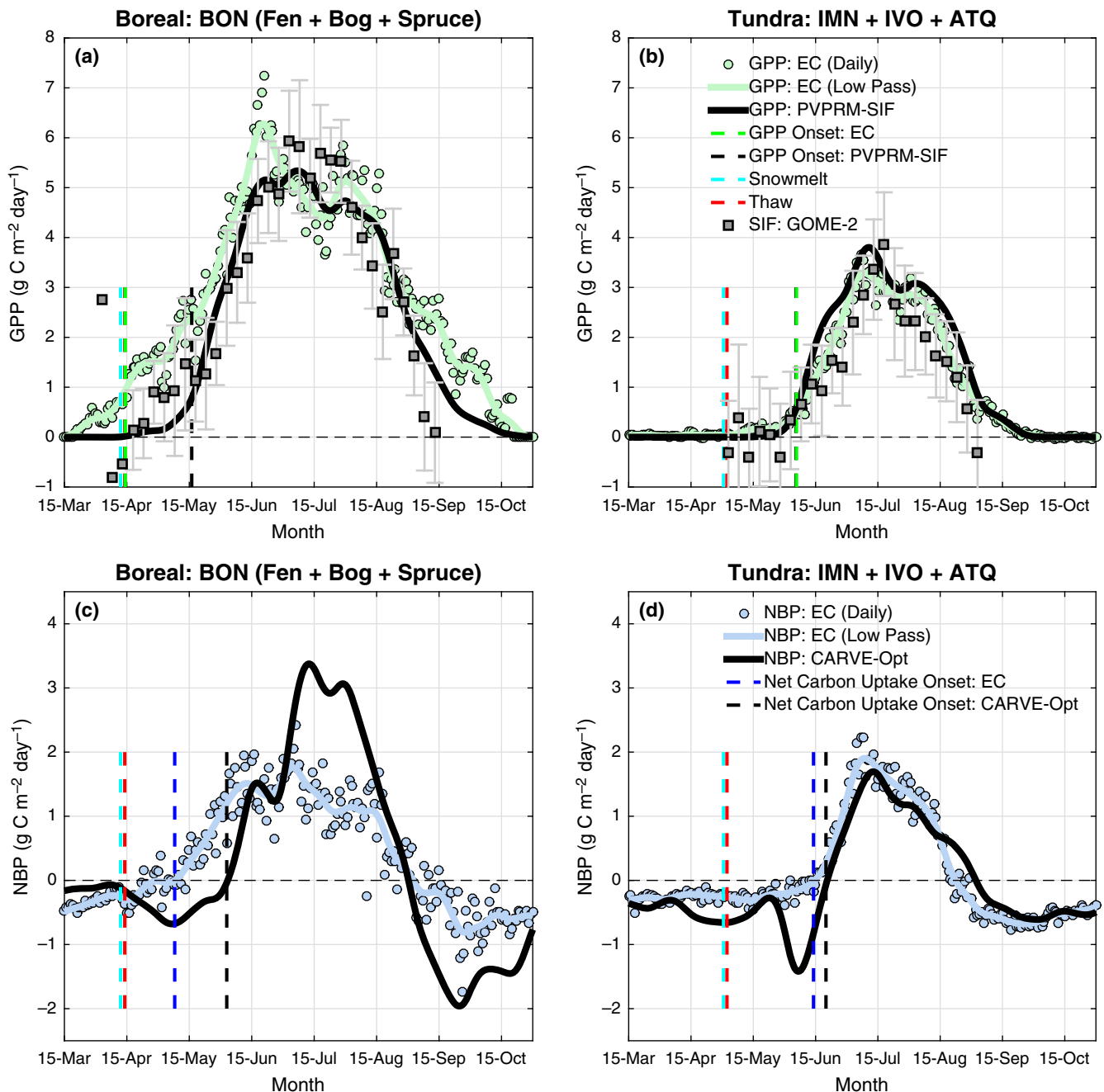


FIGURE 2 Evaluation of observationally constrained estimates of seasonal gross primary production (PVPRM-SIF GPP) (a–b) and net biome production (CARVE-Opt NBP) (c–d) against tower eddy covariance data in Interior and Northern Alaska, averaged from 2012 to 2014. Daily averages (symbols) and low-pass filters (lines) are shown for flux towers (green = GPP, blue = NBP) and low-pass butterworth filters (order 2, cutoff frequency = 0.1) for PVPRM-SIF (solid black, top) and CARVE-Opt (solid black, bottom). Boreal fluxes are averaged over the cluster of Spruce, Fen, and Bog sites at Bonanza Creek Experimental Forest (BON, three sites total). Tundra fluxes are averaged over the cluster of Hedge, Sedge, and Tussock sites at IMN and individual sites at IVO and ATQ (five sites total). CARVE-Opt and PVPRM-SIF are sampled at towers only for years when growing season eddy covariance data are available, which differs between sites (see Table 1). Onset dates for snow melt, thaw, GPP, and net carbon uptake shown in vertical dashed lines. Five-day mean retrievals of GOME-2 solar-induced fluorescence (SIF) and standard error sampled in a $2^{\circ} \times 2^{\circ}$ grid box surrounding eddy covariance tower and normalized by PVPRM-SIF are shown in gray in a–b. Thaw, GPP, and net C sink-onset dates are provided in Table 2. Positive NBP values denote net sink of atmospheric CO₂. Seasonal C flux dynamics are well represented by observationally constrained estimates in tundra but show delayed spring onset compared to the black spruce forest

(DOY 136 in Boreal Interior). May 15 also roughly corresponds to the mean date of first CARVE CO₂ observations (DOY 128), ensuring that CARVE-Opt NBP results are consistent with available spring

observations. Mean spring GPP decreases at a rate of -0.8 ± 0.03 gC/m² for every 2 weeks of delayed thaw ($R^2 = .44$). All ecosystems exhibit similar relationships, but the sensitivity of reduced GPP to delayed thaw

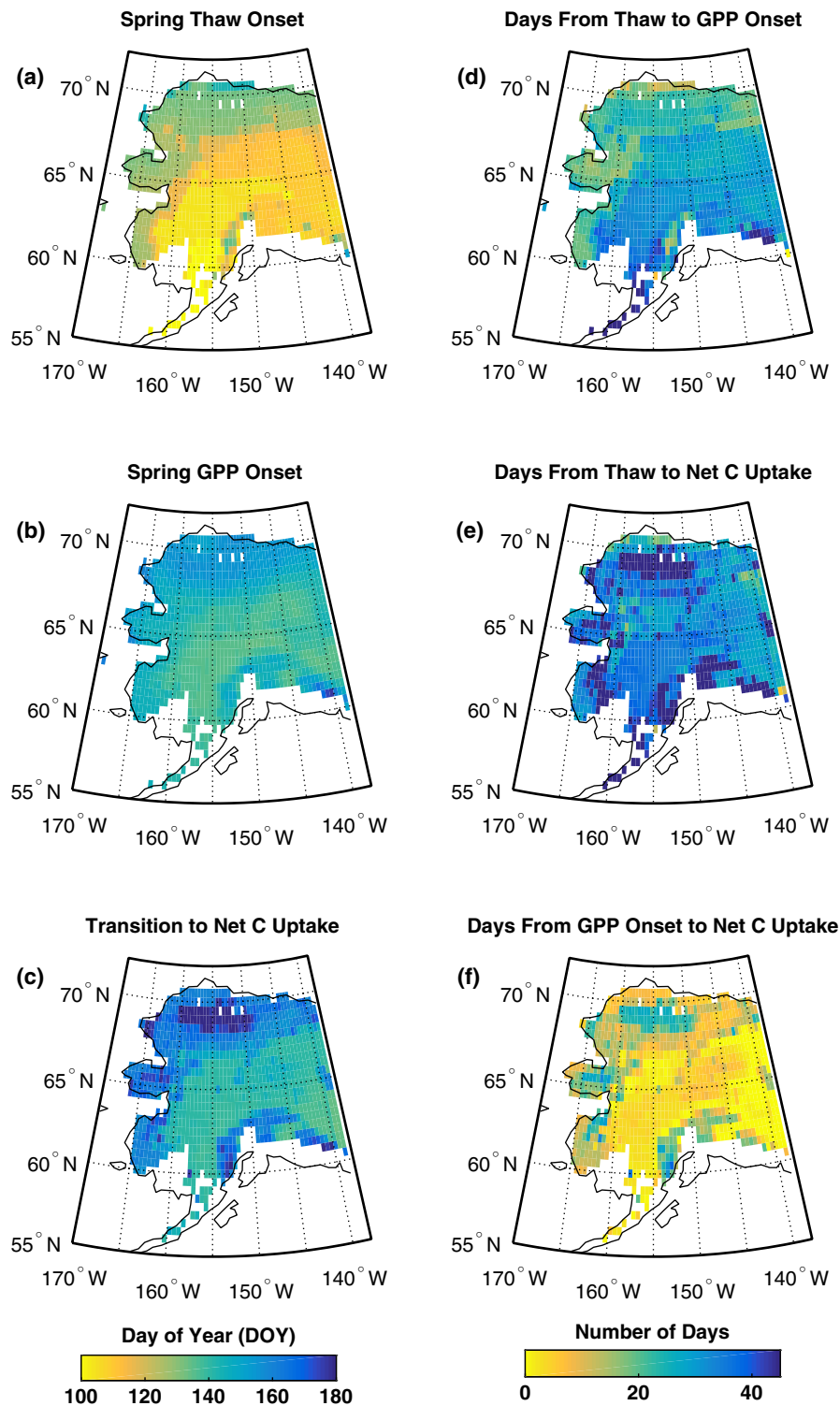


FIGURE 3 Maps showing spatial patterns of spring-onset dates for landscape thaw, GPP, and net C uptake at regional scale for Alaska. (a) Spring thaw date, representing the transition of the landscape from frozen to thawed conditions, is derived from AMSR-E and SSM/I. (b) Spring GPP onset, representing the date when ecosystem GPP reaches 10% of the growing season peak, is derived from PVPRM-SIF. (c) Net C uptake, representing the spring transition from net C source in winter to net C sink in summer, is derived from CARVE-Opt, a regional flux inversion for Alaska constrained by airborne CO₂ profiles. Number of days between thaw and GPP onset (d), thaw and net C uptake (e), and GPP onset to net C uptake (f) are estimated as the difference between maps in a–c. Values in a–c are plotted as day of year (DOY). This shows similar spatial patterns of the timing of spring thaw and GPP onset, and a decrease in the number of days from thaw to spring onset moving from south to north along the boreal–tundra gradient

TABLE 2 Mean (\pm SD) [Min Max] dates (DOY) for regional estimates of spring snow melt, landscape thaw, GPP onset, C sink onset, and mean time lags (days) between thaw and GPP onset and between thaw and C sink onset. Results are shown at eddy covariance (eddy covariance) towers (eddy covariance observations shown in parentheses), EPA Level II and III ecoregions (rows 3–7), and for combined tundra and boreal ecoregions (rows 8–9)

Region	Snow melt date (DOY)	Thaw date (DOY)	GPP-onset date (DOY)	C Sink-onset date (DOY)	Thaw-GPP lag (days)	Thaw-C sink lag (days)	GPP-C sink lag (days)
Tundra: IMN-ATQ-IVO	121	122	155 (155)	170 (164)	33 (33)	48 (42)	15 (9)
Boreal: BON	102	104	136 (104)	153 (128)	32 (0)	49 (24)	17 (24)
Tundra North Slope	117 \pm 12; [84.2 153]	133 \pm 5; [118 148]	154 \pm 3; [144 160]	167 \pm 9; [147 182]	20 \pm 5; [9 31]	36 \pm 10; [16 50]	14 \pm 8; [2 27]
Tundra Brooks	112 \pm 8; [94 127]	126 \pm 5; [113 132]	150 \pm 3; [142 156]	161 \pm 8; [139 180]	24 \pm 4; [17 33]	35 \pm 7; [16 50]	11 \pm 6; [−3 25]
Tundra Southwest	103 \pm 12; [77 131]	119 \pm 15; [85 135]	146 \pm 5; [137 164]	159 \pm 11; [139 178]	26 \pm 11; [7 57]	41 \pm 10; [13 76]	13 \pm 8; [−3 36]
Boreal Interior	98 \pm 8; [78 121]	110 \pm 7; [96 129]	139 \pm 3; [135 149]	144 \pm 7; [137 175]	29 \pm 5; [16 42]	34 \pm 6; [16 61]	5 \pm 5; [−2 30]
Boreal Mountain	102 \pm 11; [66 136]	112 \pm 7; [89 152]	142 \pm 5; [135 177]	146 \pm 12; [133 188]	30 \pm 6; [−2 67]	34 \pm 11; [5 82]	4 \pm 9; [−17 38]
Tundra: North Slope + Brooks + Southwest	112 \pm 12; [77 153]	127 \pm 10; [85 148]	151 \pm 5; [137 164]	163 \pm 10; [139 182]	23 \pm 7; [7 57]	37 \pm 9; [13 76]	13 \pm 7; [−3 36]
Boreal: Interior + Mountain	100 \pm 10; [66 136]	111 \pm 7; [89 152]	141 \pm 5; [135 177]	145 \pm 10; [133 188]	29 \pm 6; [−2 67]	34 \pm 9; [5 82]	4 \pm 7; [−17 38]

date is three times stronger on average in boreal forests (e.g., -0.9 ± 0.09 gC m⁻² day⁻¹ per 2 weeks) than in tundra (e.g., -0.3 ± 0.04 gC m⁻² day⁻¹ per 2 weeks). Spring NBP also decreases with later thaw (-0.5 ± 0.02 gC m⁻² day⁻¹, Figure 4c), but shows higher consistency (within a factor of 2 difference) across ecosystems (tundra = -0.2 ± 0.06 gC m⁻² day⁻¹; boreal = -0.4 ± 0.04 gC m⁻² day⁻¹). As such, the sensitivities of GPP and NBP to thaw in tundra are of similar magnitude while sensitivities for boreal forest are 2–3 times weaker for NBP than GPP. The relationship between spring GPP and NBP for tundra and boreal ecosystems is summarized in Figure 4d. Overall, NBP increases at half the rate of GPP ($y = \times 0.5x + 0.5$), but with higher overall sensitivity in tundra (-0.7 ± 0.09) than boreal (-0.35 ± 0.02), and reduced sensitivity for lower GPP (tundra = -0.6 ± 0.1 ; boreal = -0.5 ± 0.1).

The reduced sensitivity of NBP to GPP in boreal points to TER onset as a key factor, also driven by thawing, which offsets the initial spring GPP. Aggregated plots of TER (Figure 5a) show an initial increase between snow melt and landscape thaw (DOY 100 ± 10 and 111 ± 7 , respectively), ~ 4 weeks prior to GPP onset (DOY 141 ± 5). The transition from onset of GPP to net C uptake (DOY 145 ± 10) is short throughout boreal forests (Figure 3f), but the C uptake rate is initially slow (-1.2 gC m⁻² month⁻¹) due to synchronous increases in GPP and TER following GPP onset. C uptake accelerates in early June as respiration levels off with substrate depletion and GPP fully recovers from winter.

Regional mean-onset dates for boreal GPP (DOY 141 ± 5) and net C uptake (DOY 145 ± 10) are early, and corresponding lag time (4 ± 7 das) short, compared to eddy covariance observations at BOR (DOY 104 and 128, and 24 day lag, respectively). However, the lag time is highly variable at regional scale (± 7 days). Furthermore, the lag time sampled at the tower (17 days) corresponds more closely with eddy covariance data (20 days). This suggests that the dynamics driving net C uptake onset are not well captured by CARVE-Opt at BOR and potentially other boreal locations, due to sparse airborne CO₂ coverage before mid-May and coarse spatial resolution of CARVE-Opt. Enhanced airborne sampling after mid-May leads to improved representation of the transition from GPP to net C uptake onset.

Respiration offsets an even larger fraction of spring GPP in tundra (Figure 5b) due to early respiration in mid-April (similar timing to boreal) and delayed GPP onset (10 days later than boreal). The timing of TER onset corresponds closer to the mean-onset date of snow melt (DOY 112 ± 12) than landscape thaw (DOY 127 ± 10), consistent with onset of subnivean respiration. The GPP delay also causes a slight phase shift between GPP and TER seasonal cycles, increasing the transition time from the onset of GPP (151 ± 5) to net C uptake (163 ± 10 days) by a factor of 3 compared to boreal (13 ± 7 days). Longer transition times are found throughout western and North Slope tundra, with longest times just north of the Brooks Range (Figure 3f). Consequently, the transition time from thaw to net C uptake is delayed in tundra by 37 ± 9 days (Figure 3e), similar to the boreal transition (34 ± 9 days), but leads to a 50% higher NBP following the transition to net C uptake (-1.8 gC m⁻² month⁻¹). Regional

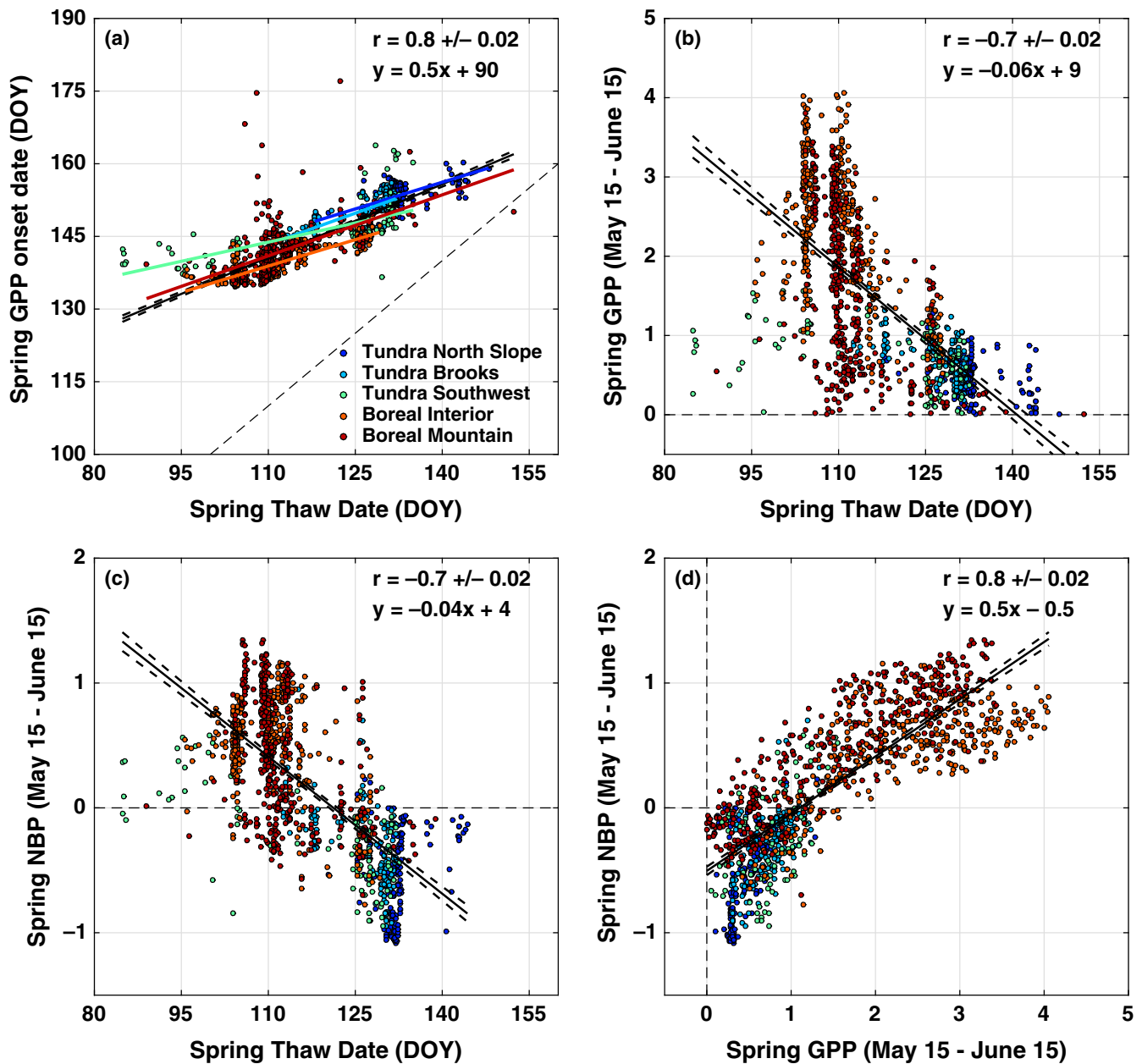


FIGURE 4 Relationship between spring CO_2 flux and landscape thaw. Scatter plots show regressions of (a) spring GPP-onset date vs. thaw date, (b) Mean spring GPP from May 15 to June 15 vs. thaw date, (c) Mean spring NBP from May 15 to June 15 vs. thaw date, and (d) mean spring NBP vs. GPP ($\text{gC m}^{-2} \text{day}^{-1}$). Positive NBP denotes net C uptake by plants. Colors denote the five ecoregions of interest. Regression lines are plotted for each ecoregion in (a). Regression statistics are reported for all points combined in each subpanel. We note several emergent patterns: (i) the relationship between dates of spring GPP onset and landscape thaw are consistent across ecoregions, (ii) the magnitude of GPP is more sensitive to thaw date in boreal than tundra, (iii) NBP magnitude is equally sensitive to thaw date in boreal and tundra, and (iv) NBP is more sensitive to GPP change, and hence thaw date, in tundra

mean C flux-onset dates and lag times in tundra are consistent and within the uncertainty of eddy covariance data analyzed in this study.

3.3 | Analysis against other CO_2 inversion systems

Our reported spring C uptake patterns are specific to CARVE-Opt, which represents an estimate of Alaskan regional-scale dynamics

complementary to global inversions due to the proximity of airborne CO_2 measurements to regional flux and the higher resolution of atmospheric transport. Using CARVE-Opt as a benchmark, we compare the timing and depth of spring C uptake to global inverse estimates derived from near-surface CO_2 observations from CT2016 and Jena4.1 (Figure 5c–d), which are reported daily, and satellite column data from CMSb7.3 (Figure 5e–f), which is reported monthly (15th of month).

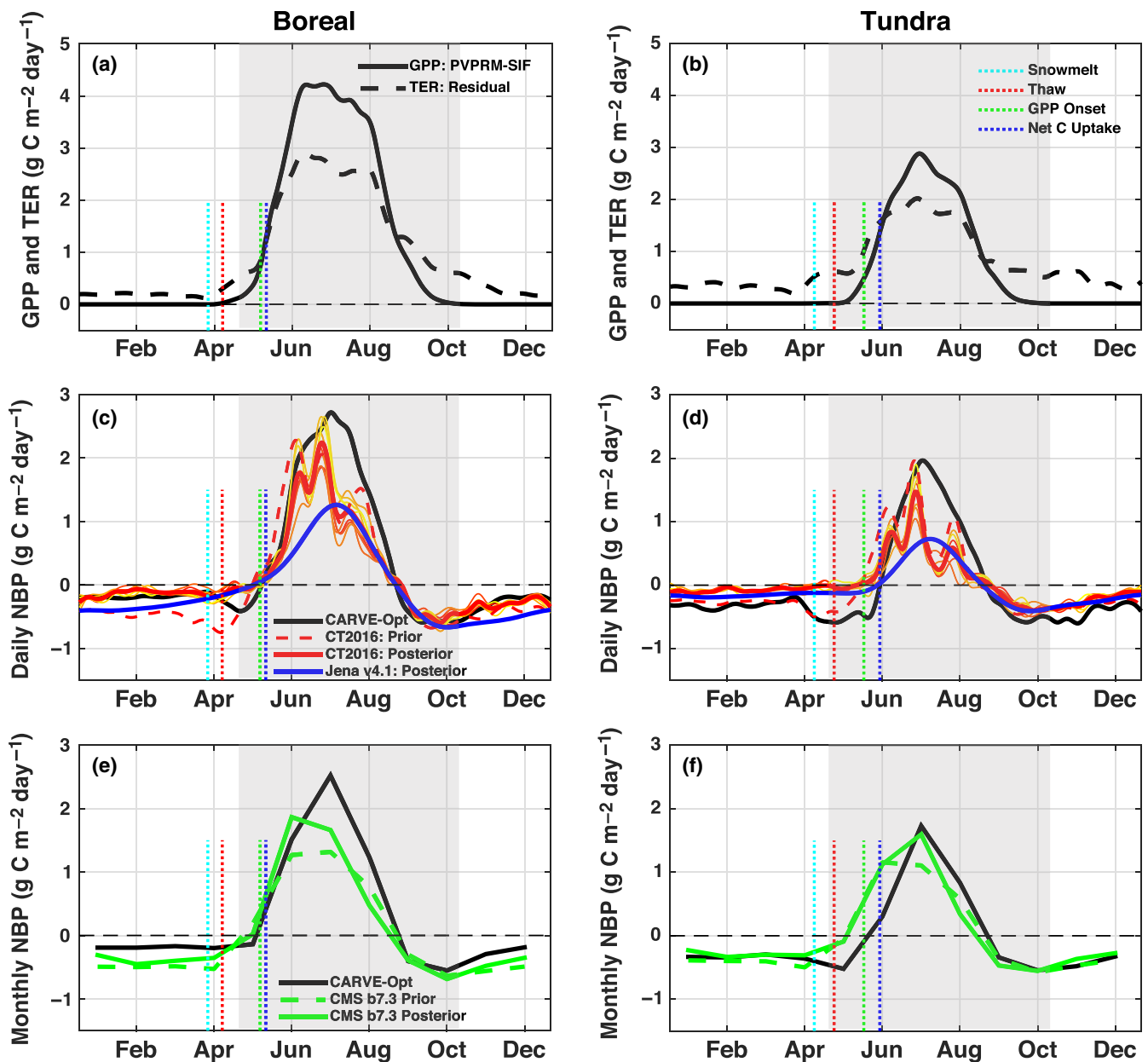


FIGURE 5 Seasonal GPP and NBP patterns for boreal and tundra ecoregions. (a–b) Seasonal GPP (solid) from PVPRM-SIF and terrestrial ecosystem respiration (TER, dashed) from the residual of CARVE-Opt NBP and PVPRM-SIF GPP. (c–d) Seasonal NBP derived from daily averages of CARVE-Opt (black), CT2016 ensemble (red), Jena v4.1 (blue) posterior fluxes, and CT2016 prior fluxes (red dashed). (e–f) Seasonal NBP (positive denotes net sink) derived from monthly averages of CARVE-Opt (black) and CMS b7.3 posterior (green solid) and prior (green dashed) fluxes. Results for boreal ecoregions shown in the left column and tundra in the right column. X-axis labels represent middle of month. Shaded area shows valid range of climatological CARVE-Opt NBP for the period 2012–2014, representing CARVE campaign start and end dates (May 7 and October 20 on average). Vertical dashed lines denote mean date of snow melt (cyan), landscape thaw (red), GPP onset (green), and net C uptake (blue) for each ecoregion. CT2016 and Jena v4.1 are global inverse estimates derived from near-surface CO₂ observations. CMS b7.3 is derived from satellite column integrated CO₂. CT2016 results are shown for eight ensemble runs driven by the different combination of fossil fuel, ocean, and biosphere priors. The results show variable patterns of the amplitude and timing of seasonal CO₂ exchange for each ecoregion and inversion method

In boreal forests, global and regional inversions show general agreement of earlier and greater uptake compared to tundra. The inversions also show remarkable agreement in spring net C uptake onset and transition back to net source in fall. Global inversions do not show a boreal respiration pulse as seen in CARVE-Opt in mid-May in the 3-year average, although Jena4.1 reflects this in

individual years. Likewise, the presence of this pulse in CARVE-Opt is predicted by PVPRM in all years but only confirmed by CARVE airborne observations in 2013. The pulse is not detected in eddy covariance data at BON-Spr or BON-Bog but is observed at BON-Fen (Figure S2). Thus, the repeatability of this pulse over multiple years and at regional scale is unclear.

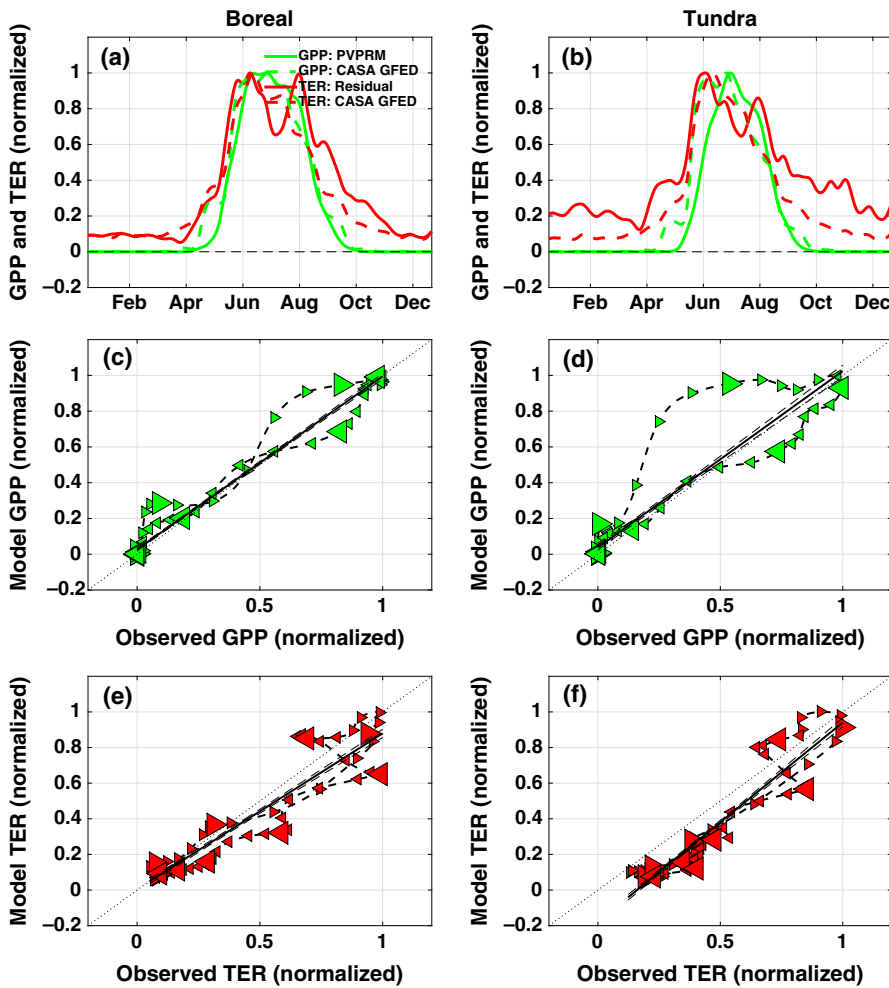


FIGURE 6 Errors in predicted seasonal GPP and TER. (a–b) Seasonal time series of daily optimized (solid) and simulated (dashed) GPP (green) and TER (red). (c–d) Regression of simulated and optimized GPP. (e–f) Regression of simulated and optimized TER. Optimized GPP is taken from PVPRM-SIF and TER as the residual of CARVE-Opt NBP and PVPRM-SIF GPP. Values are reported every 5 days, with large symbols denoting mid-month. Model fluxes are taken from CASA GFED3. The results show a positive bias in spring GPP in boreal and tundra ecosystems, driven by early GPP onset, which leads to an early transition from net C source to sink compared to CARVE-Opt

Jena4.1 estimates a smaller rate and depth of uptake in the early growing season compared to CARVE-Opt and CT2016. The smooth transition from March to July aligns well with BON-Spr but not with BON-Fen or BON-Bog. The small seasonal amplitude in Jena4.1 is likely related to the model prior which, in contrast to both CARVE-Opt and the other global inversions, uses a constant zero prior in place of a modeled prior.

The relative seasonal patterns across inversions are similar for tundra, but here, we give more weight to CARVE-Opt due to the high agreement in phase and amplitude with eddy covariance data (Figure 2d). CMSb7.3 and CT2016 capture the depth and rate of spring uptake. The sustained tundra efflux from late April to early June is absent from all methods. The true magnitude of the spring tundra source likely falls somewhere between CARVE-Opt ($\sim 0.5 \text{ gC m}^{-2} \text{ day}^{-1}$) and surface inversions ($< 0.1 \text{ gC m}^{-2} \text{ day}^{-1}$) as suggested by eddy covariance data ($\sim 0.25 \text{ gC m}^{-2} \text{ day}^{-1}$), although we note a stronger pulse at the representative tundra site of IVO (Figure S2g), which peaks at $0.5 \text{ gC m}^{-2} \text{ day}^{-1}$ in mid-June. Nevertheless, CT2016 and Jena4.1 capture the delayed timing of spring uptake in tundra. In contrast, CMSb7.3 has a pronounced early spring bias in tundra of ~ 3 weeks.

We investigate the CMSb7.3 spring bias in more detail by comparing posterior and prior NBP. Prior NBP is prescribed from CASA-

GFED3, shown in Figure 5e,f. Seasonal NBP amplitude in CMSb7.3 is much improved compared to CASA-GFED3. However, the timing of the spring and fall transitions is generally fixed relative to CASA-GFED3, which is early compared to CARVE-Opt in spring. In contrast, CT2016 shows a shift in both the seasonal amplitude and phase relative to its prior, CASA-GFED4.1. Although CASA-GFED4.1 also has an early bias, CT2016 forces a delay in net C uptake onset in boreal and tundra regions in closer agreement with CARVE-Opt across the range of fossil fuel, ocean, and biosphere priors in the CT2016 ensemble. The inversion does not have substantial impact on the seasonal amplitude or duration of drawdown following peak uptake, which is underestimated compared to CARVE-Opt. An explanation of spring timing difference across inverse methods is provided in the Discussion.

Finally, we examine the source of the early spring bias in CASA-GFED. Previous analyses of CASA in lower latitude boreal forests characterized GPP as generally well represented in satellite-constrained diagnostic models, and that differential phasing of TER with respect to GPP is needed to accurately estimate NBP timing surrounding the growing season peak (Messerschmidt et al., 2013). Our analysis of cold northern boreal and tundra ecosystems suggests the opposite; the timing of spring TER onset is well represented in CASA-GFED, while GPP onset is systematically early in boreal and

tundra regions (Figure 6). In tundra in particular, CASA-GFED predicts an early initial GPP increase in late April, followed by a larger secondary jump in late May which increases more rapidly than suggested by PVPRM-SIF. The timing is exacerbated by the use of monthly mean-normalized difference vegetation index and APAR in CASA, causing GPP to increase more instantaneously than a monthly interpolated change.

4 | DISCUSSION

4.1 | Spring photosynthetic recovery in Alaska Tundra and Boreal Forests

Our results indicate that the timing and magnitude of spring C fluxes in Alaska are correlated with landscape thaw and ecoregion. Tundra ecosystems thaw on average 2 weeks later than boreal forests and require less time to transition to GPP onset. This pattern of later thaw and reduced lag time in tundra (23 ± 7 days) compared to boreal forests (29 ± 6 days) is consistent with eddy covariance data for eastern Canada and Sweden (Kim et al., 2012). The short time lag in Alaskan tundra, and especially North Slope tundra (20 ± 5 days), is consistent with data in Siberian tundra showing rapid physiological response to warming and snow melt, a plausible adaptation of high-latitude tundra ecosystems to the short-growing season (Arneth et al., 2006). Interior boreal forests have been found to require at least an extra week to reach 10%–20% capacity due to pigment adjustments (e.g., Ottander et al., 1995).

In Alaskan tundra, PVPRM-SIF indicates a weak physiological response for the first 2 weeks after thaw onset followed by a more rapid response, with 15% of peak annual GPP attained after 3 weeks and peak GPP after 8 weeks. Low initial GPP, especially in northern Alaska, is attributed to high radiation exposure with later thaw; incident radiation along the North Slope and Brooks Range exceeds Boreal Interior values by 20% and represents a larger percentage of peak annual radiation (82% vs. 67%). This apparent light stress, and subsequent rapid recovery, is supported by evidence from *Sphagnum* moss near Barrow, Alaska, which shows low levels of photosynthesis early in the season due to photoinhibition, then the development of subsurface moss layers and structural protection from high radiation later in the season, enabling increased photosynthetic capacity with reduced risk of light damage (Zona et al., 2011). High nitrogen (N) availability early in the growing season, driven by decreases in microbial biomass and release of N during snow melt, provides further stimulus to photosynthesis under snow and following snow melt (Brooks, Williams, & Schmidt, 1998; Larsen, Grogan, Jonasson, & Michelsen, 2007; Starr & Oberbauer, 2003). The convergence of soil thawing and seasonal phenology with latitude thus appears to reflect the efficient adaptation of high-latitude shrubby ecosystems to cold, high light, and nutrient rich environments and the need to maximize the number of growing days and soil liquid water availability during the short thaw season.

These same factors (warm temperatures and high N availability at thaw onset) also stimulate the decomposition of soil organic carbon by microbes, leading to simultaneous increases in soil respiration

(Lafleur & Humphreys, 2007; Oberbauer et al., 1998). Furthermore, competition for N by plants and microbes leads to a crash ~1 month following snow melt, such that tundra plants become N limited (Larsen et al., 2007). These studies are consistent with our finding of delayed time from GPP onset to net C uptake, roughly 2 weeks (14 ± 8 days) in the Tundra North Slope.

Although we estimate a longer time lag in boreal forests on average, we note the difference from tundra is within the statistical uncertainty, thus permitting cases where time lag is reversed and shorter in boreal forests. Evidence from mire (tundra) and pine (boreal) sites in Siberia sharing similar climate indicate a shorter time lag in the pine forest, which exhibits a rapid physiological response to above zero temperature even when there is snow on the ground (Arneth et al., 2006; Euskirchen et al., 2014). Needleleaf trees such as black spruce at Bonanza Creek show a negative lag (GPP reaches ~15% of peak prior to thaw) triggered by early warming (Figure S7), with the first nonzero GPP values occurring in the afternoon (12:00 a.m. to 03:00 p.m.), prior to onset of primary thaw, on days with above freezing afternoon air temperature and near or below freezing morning temperature (09:00 a.m.–12:00 p.m.). This early photosynthesis, at least in evergreens, represents a physiological adaptation to stress when sufficient radiation is already available and absorbed by green needles, and small amounts of plant available liquid water in soils can be transported through xylem in conifers and evaporated through leaf stomata as a cooling mechanism (Ishida, Nakano, Sekikawa, Maruta, & Masuzawa, 2001). These results suggest that sunlight, air temperature, and xylem flow may be better predictors of photosynthetic onset in evergreens than date of primary thaw. However, we note that weak levels of photosynthesis have been observed during transient freeze–thaw cycles during the spring zero curtain preceding primary thaw (Tanja et al., 2003). Diurnal freeze–thaw data may, therefore, offer a useful indicator of initial photosynthesis, provided that the resolution is fine enough ($<10 \text{ km}^2$) to distinguish between vegetation and soil landscape components.

4.2 | Limitations and uncertainties for SIF and CO₂ observations

In evaluating PVPRM-SIF and CARVE-Opt C flux patterns against eddy covariance data, we find good representation of tundra C flux seasonality and earlier GPP onset in boreal forests, but a potential late-onset bias in the timing of spring onset of GPP and net C uptake in boreal forests. We analyze temperature forcing for a cold bias in PVPRM, which might lead to late GPP onset, but find good agreement to observed temperature at Bonanza Creek (Figure S9). The following limitations in our use of satellite SIF for constraining spring onset of evergreen photosynthesis provides a more likely explanation: (i) GOME-2 overpass time, (ii) assumed SIF-GPP linearity, (iii) monthly aggregation.

First and foremost, we note that the GOME-2 SIF late morning overpass in Alaska (~11:30 a.m.) hinders the observation of early season peak daytime photosynthesis in high-latitude evergreens,

which can occur even if morning or daily mean temperatures are below freezing (as discussed above), or under transitional (AM frozen, PM thawed) thaw events (Kim et al., 2012). The switch from negative to positive SIF signals at Bonanza Creek occurs following a significant rise in morning temperature of 3–5°C above freezing and near primary thaw (Figure S7). As such, PVPRM-SIF is unlikely to capture early GPP onset in boreal evergreen forests when constrained solely by spaceborne spectrometers with morning overpasses. Instruments with midday overpass, such as TROPOMI and OCO-2 (e.g., Guanter et al., 2015), are better suited to capture daytime signals, but inadequate by themselves to detect transitional thaw events, and thus cannot represent true daily mean SIF. OCO-2 also lacks the temporal resolution (16 day repeat cycles) to resolve the spring transition (e.g., Sun et al., 2018). Ideally, a harmonized product combining spatially resolved, polar-orbiting instruments with morning (GOME-2, SCIAMACHY) and midday (TROPOMI, OCO-2) is needed.

It is important to note, however, that SIF is not as well correlated with photosynthesis during the early growing season when leaf-level photochemistry precedes increasing SIF emissions (Springer et al., 2017). In evergreens, the SIF–GPP relation changes seasonally with changes in nonphotochemical quenching (NPQ) and shifts in carotenoid pigments during transition seasons (Ottander et al., 1995). Increasing pigmentation in fall functions to shed more absorbed energy as NPQ than SIF over winter months (Demmig-Adams & Adams, 1996; Müller, Li, & Niyogi, 2001; Ottander et al., 1995; Porcar-Castell, 2011) and in early spring with increasing exposure to harmful radiation (Arneeth et al., 2006). Increases in absorbed light and temperature in spring during the cold dehardening period cause relative declines in carotenoid pigments and increases in chlorophyll concentrations, leading to increasing photosynthetic activity, reduced NPQ, and increased dissipation of absorbed light as SIF (Springer et al., 2018; Wong & Gamon, 2015). The increase in SIF and GPP in evergreens is gradual due to the gradually changing pigment ratios of carotenoids and chlorophyll (Wong & Gamon, 2015). Although a recent analysis of GOME-2 SIF has supported a temperature triggered early-onset mechanism at pan-Arctic scale (Walther et al., 2016), our results suggest that true onset may occur several weeks earlier. We, thus, recommend the use of additional remote-sensing indices such as chlorophyll carotenoid index (CCI) and photochemical reflectance index (PRI) with midday and morning SIF to interpret the full dynamical range of photosynthesis during spring onset (Springer et al., 2017).

This research has also demonstrated that our method to aggregate GOME-2 SIF retrievals by month and biome class, with linear interpolation between values (Luus et al., 2017), is inadequate to resolve spring transitions at high latitudes. Analysis of 5-day mean SIF retrievals, for example, suggest earlier photosynthetic recovery at BON than in the regional average of Alaskan evergreens (Figure 2a). Future efforts to reduce these errors and interpret patterns of thaw vs. C flux onset requires at a minimum nonlinear interpolation methods for monthly SIF and ideally more spatiotemporal explicit application of satellite SIF data in light use efficiency models.

More sustained early season, spatially intensive sampling of airborne CO₂ (Parazoo et al., 2016) and longer term eddy covariance fluxes and from additional sites in high northern boreal forests is also needed.

SIF-based GPP-onset biases in forests feed into NBP calculations and contribute to errors in seasonal amplitude and timing. NBP optimization by CARVE CO₂ observations alleviates most errors at regional scale, but a few remaining grid-scale errors persist at tundra and boreal locations. These are attributed to four key factors. First, as discussed above, is the high spatial variability and biome dependence of net C uptake onset. This has an especially large impact on NBP at tundra sites (IMN, IVO) located along the border of Brooks and North Slope subregions. Second is the small sample size of boreal forest sites, represented only by BON-Spr. BON-Spr is also unique in its sudden shift in summer NBP magnitude during the 2 years of overlap with CARVE-Opt, switching from a large summer sink from 2010 to 2012 to a small or neutral summer sink from 2013 to 2016 (Figure S8). We suspect that the reduced summer sink is related to a local respiration source from underlying permafrost and thermokarst near the tower, which is undetected by CARVE flights. Third is the lack of consistent airborne CO₂ flights from early April to late May during the eddy covariance NBP transition. Thus, our NBP estimate during this period relies on PVPRM, which estimates a delayed net C uptake onset following late GPP onset. Fourth is the relatively short 3-year record. Significant natural year-to-year variability in the onset of thaw, phenology, and gross/net C uptake at ecosystem and regional scale is common in Alaska (e.g., Commane, Lindaas et al., 2017; Kim et al., 2012) and makes it difficult to examine climatological spatial patterns over short records. Although the focus of this research is regional scale and thus limited by data availability, we note that ongoing measurements of satellite SIF and airborne CO₂ from the recent NASA Arctic-Boreal Vulnerability Experiment (ABOVE, <https://above.nasa.gov>) will provide a longer period of record to analyze interannual variability.

4.3 | Limitations and uncertainties for eddy covariance observations

We also note the factor of 2–3 overestimation of GPP at ATQ by PVPRM-SIF. This error is attributed to two factors: (i) a calibration/validation inconsistency, with PRVPM parameters calibrated using year-round 2005 ATQ data but validated against 2014 ATQ data, (ii) representativeness of eddy covariance. The first factor would cause a high bias only if GPP and NBP in 2005 were higher than data in 2014, shown here. Although data in 2005 are not available for comparison, we can infer the tendency of GPP in 2005 vs. 2014 using a very simple model of GPP as a function of thawing degree-days (TDD), estimated as the sum of the mean daily temperature above 0°C and for which we have site level data available from 2005 to 2014. This model assumes higher peak GPP for larger TDD. We find a TDD of 650 days in 2005 and 563 days in 2014, indicating higher productivity in 2005. Previous work using chamber data shows higher GPP in 2013 than in 2014 at ATQ (Davidson et al., 2016),

consistent with higher TDD (720 days). These findings indicate higher GPP in 2005, which supports a calibration bias at ATQ and argues for an updated calibration of PVPRM using the longer record of data at existing eddy covariance towers (Luus & Lin, 2015) and inclusion of new tundra and boreal towers (<http://ameriflux.lbl.gov/data/>).

With regard to the second factor (representativeness), eddy covariance is the most direct measurement of ecosystem fluxes available; however, several uncertainties should be considered in the interpretation of our results: (i) the tower footprint ($\sim 10^0$ km²) is large compared to individual tree canopies (<5 m), making it a challenge to disentangle contributions from different vegetation types and C sources in heterogeneous Alaskan landscapes. For example, moss contributions to total NBP range from 25% to 60% in mixed tundra landscapes (Zona et al., 2011) such as seen at Ivotuk (tussock-sedge, dwarf-shrub, and moss tundra) and Atqasuk (sedge, grass, mosses, and dwarf sedge). At the BON cluster, nearby thermokarst permafrost emissions have a substantial influence of C fluxes observed at BON-Spr (Figure S8); (ii) the tower footprint is much smaller compared to footprints for PVPRM-SIF ($\sim 10^2$ km²), CARVE-OPT ($\sim 10^3$ km²), and aggregated SIF soundings ($\sim 10^4$ km²). Although some effort is made to capture subgrid variability by combining tower clusters (e.g., IMN, BON) and similar ecosystems (e.g., Figure 2) and by examining sensitivity to spatial resolution (e.g., Figure S1), we caution that spatial representativeness issues remain in the flux tower-model comparisons. Airborne eddy covariance surveys provide a viable option to increase footprint size toward regional scale (Wolfe et al., 2018); (iii) flux partitioning of eddy covariance NEE into GPP and TER also carries large uncertainties and can yield very different results depending on method (e.g., Figure S1). This uncertainty in itself may explain the short time lags between thaw and GPP observed at Bonanza Creek. More work is needed to understand the sensitivity of nighttime- vs. daytime-partitioning techniques in Alaska and impact on GPP seasonal onset/offset and amplitude, in particular as a function of length of day, and to compare flux-partitioning algorithms to measured respiration from dark chambers across the Arctic.

4.4 | Implications for top-down and bottom-up estimates of net carbon exchange

Our results also indicate similar time lags from thaw to net C uptake onset in tundra and boreal (~ 5 weeks), such that net C uptake occurs later in tundra, with exact timing depending on vegetation type (wet sedge, heath, tussock) (Figure S2). Delayed tundra uptake is captured in global inverse models, but with net C uptake onset too early in spring and too shallow in summer. Further assessment of CMSb73, which has the most severe spring timing bias, indicates a link to early net C uptake onset in the CASA-GFED prior and exacerbated by the estimation of monthly scale factors for net exchange and limited seasonal coverage of satellite observations. Since CMSb7.3 and CT2016 share a similar prior in CASA-GFED, we can identify three additional factors contributing to difference in spring timing across inverse

methods: (i) observation source, (ii) optimization method, indicating the application of scale factor correction to model priors, and (iii) optimization window, representing the length of time in which scale factors are estimated in the optimization procedure.

Regarding the first factor (observation source), CT2016 assimilates in situ data, which have continuous year-round coverage, whereas CMSb7.3 assimilates satellite observations derived from reflected sunlight, which have seasonal-dependent coverage over high latitudes. As such, the correction to fluxes occurring during polar winter and during snow cover in spring is minimal in CMSb7.3, especially for North Slope and Brooks tundra. However, the enhanced spatial coverage of GOSAT in summer provides a boost in peak summer uptake compared to CASA-GFED. Combining high-latitude flask, airborne, and satellite observations into a consistent global inversion framework will improve seasonal and spatial constraints and retain the advantage of dense satellite-observational coverage in summer.

Regarding the second factor (optimization method), Jena4.1 has no prior flux information and thus does not apply scale factor correction. This flexible approach produces an accurate representation of the seasonal transition in spring and fall, but with a trade-off in seasonal amplitude. CT2016 and CMSb7.3 optimize scale factors for NBP at regional and grid scale, respectively, as corrections to prior fluxes, and thus are more strongly weighted by prior information. This less flexible approach produces more accurate representation of seasonal amplitude but leads to errors in the seasonal transition timing, which is strongly weighted by prior information under reduced observational coverage.

Regarding the third factor (optimization window), CMSb7.3 uses a monthly window; CT2016 uses a weekly (8 day) window. We propose that the smaller 8-day window allows more flexibility for data assimilation to adjust the spring transition date, which greatly affects the interpretation of seasonal C uptake dynamics. Alternative inverse methods which estimate scaling factors for gross fluxes (Deng, Jones, O'Dell, Nassar, & Parazoo, 2016) or persistent grid-scale biases (Lokupitiya et al., 2008; Parazoo, Denning, Kawa, Pawson, & Lokupitiya, 2012) permit a shift in seasonal NBP phase relative to prior information.

Early C uptake bias in CASA-GFED is consistent with CMIP5 model estimates of seasonal NBP in Alaska, which predict spring net C uptake onset to occur by an average of 18 days earlier than estimated by CARVE-Opt, with 7 of 10 models showing early bias exceeding 15 days, and three models showing a bias exceeding 1 month (Commane, Lindaas et al., 2017). In attributing the early C uptake bias, our analysis of GPP and TER fluxes in CASA-GFED indicates an accurate representation of the timing of TER in spring consistent with subnivean respiration, which is simulated in CASA-GFED as a function of soil moisture and temperature (Potter, Klooster, & Genovese, 2013) and in PVPRM as a function of soil temperature (Luus & Lin, 2015). Our results, therefore, suggest early GPP onset as the primary culprit in tundra ecosystems. Satellite-constrained light use efficiency models that prescribe green biomass using reflectance-based vegetation indices typically predict earlier GPP onset

and larger spring C uptake in cold climate ecosystems compared to the same models constrained by SIF (Luus et al., 2017; Commane, Lindaas et al., 2017). Prognostic and diagnostic models used in CMIP5, IPCC, and NACP reports also have a well-known early spring GPP bias (Peng et al., 2015), especially for temperatures below freezing (Schaefer et al., 2012). It is critical for these models to account for survival adaptation under repeated exposure to frost, cold, and frozen soils, which limits root uptake of water and stomatal conductance (Bergh et al., 1998; Strand & Öquist, 1985; Waring & Winner, 1996) and allows cold-adapted plants to avoid spring frost damage after budburst (Jeong, Medvigy, Shevliakova, & Malyshev, 2012, 2013) and high radiation following snow melt-inhibiting photosynthetic C uptake (Zona et al., 2011), thus delaying or reducing initial GPP. Other factors such as incorrect prescription of plant functional type also have important effects. Some models such as LPJ-GUESS simulate herbs (grasses) as a proxy for tundra vegetation which in reality may consist largely of shrubs. Grasses have a low-growing degree-day sum threshold for leaf onset and high light use efficiency which may explain early GPP onset in tundra in earth system models. The same issue also applies to conifers and diffuse-porous broadleaves, to which most boreal zone broadleaves belong. Our regional and site-level results support low levels of photosynthesis in tundra initially following snow melt and leaf out as well as longer time lag of ~3 weeks for full phenological recovery.

4.5 | Outlook

Climate models disagree on the trajectory of C balance in northern terrestrial ecosystems under future warming. The advance of spring C uptake observed over the past several decades in these ecosystems is a key climate change metric, but subjected to high uncertainty in ecosystem model simulations, which systematically predict early growing season onset. Our results point to landscape thawing as a key driver of seasonal C cycle dynamics in cold northern ecosystems, and a likely factor contributing to early spring C flux biases reported in ecosystem models used in IPCC climate assessment reports for projections of future climate. Failure to account for cold season soil and biochemical processes will lead to biased model and empirical-based estimates of pan-Arctic C sinks which produce too strong of biogenic uptake. This would affect estimates of the timing and magnitude of the permafrost C feedback. Next steps are to quantify sensitivity of (i) spring thaw to meteorological inputs and soil physical processes and (ii) GPP onset to biological processes such as dehardening, xylem flow, and budburst.

ACKNOWLEDGEMENTS

We thank the two anonymous reviewers for comments/suggestions that significantly improved this paper. CarbonTracker CT2016 results provided by NOAA ESRL, Boulder, Colorado, USA, from the website at <http://carbontracker.noaa.gov>. We acknowledge the role of CIRES/NOAA team in providing the dataset necessary for the inversions and post modeling validation. Some of the research described

in this paper was performed for CARVE, an Earth Ventures (EV-1) investigation, under contract with NASA. Funding for the Innavit flux towers is provided by the National Science Foundation Arctic Observation Network program (Grant 1503912) and for the boreal flux towers by the US Geological Survey Climate Research and Development Program. A portion of this research was carried out at the Jet Propulsion Laboratory, California Institute of Technology, under contract with NASA. D Zona is supported by the Office of Polar Programs of the National Science Foundation (NSF) (award number 1702797), by the National Aeronautics and Space Administration, by the ABoVE (NNX15AT74A; NNX16AF94A) Program, and by European Union's Horizon 2020 research and innovation program under grant agreement (No. 727890) © 2017. All rights reserved.

ORCID

Nicholas C. Parazoo  <http://orcid.org/0000-0002-4165-4532>

Donatella Zona  <http://orcid.org/0000-0002-0003-4839>

REFERENCES

- Arneth, A., Lloyd, J., Shibistova, O., Sogachev, A., & Kolle, O. (2006). Spring in the boreal environment: Observations on pre- and post-melt energy and CO₂ fluxes in two central Siberian ecosystems. *Boreal Environment Research*, 11, 311–328.
- Badeck, F. W., Bondeau, A., Bottcher, K., Doktor, D., Lucht, W., Schaber, J., & Sitch, S. (2004). Responses of spring phenology to climate change. *New Phytologist*, 162, 295–309.
- Barichivich, J., Briffa, K. R., Myneni, R. B., Osborn, T. J., Melvin, T. M., Ciais, P., . . . Tucker, C. (2013). Large-scale variations in the vegetation growing season and annual cycle of atmospheric CO₂ at high northern latitudes from 1950 to 2011. *Global Change Biology*, 19(10), 3167–3183. <https://doi.org/10.1111/gcb.12283>
- Bergh, J., McMurtrie, R. E., & Linder, S. (1998). Climatic factors controlling the productivity of Norway spruce: A model-based analysis. *Forest Ecology and Management*, 110(1–3), 127–139. [https://doi.org/10.1016/S0378-1127\(98\)00280-1](https://doi.org/10.1016/S0378-1127(98)00280-1)
- Bhatt, U. S., Walker, D. A., Reynolds, M. K., Comiso, J. C., Epstein, H. E., Jia, G., . . . Webber, P. J. (2010). Circumpolar Arctic tundra vegetation change is linked to sea ice decline. *Earth Interactions*, 14(8). <https://doi.org/10.1175/2010EI315.1>
- Black, T. A., Chen, W. J., Barr, A. G., Arain, M. A., Chen, Z., Nesic, Z., . . . Yang, P. C. (2000). Increased carbon sequestration by a Boreal deciduous forest in years with a warm spring. *Geophysical Research Letters*, 27(9), 1271–1274. <https://doi.org/10.1029/1999GL011234>
- Bloom, A. A., & Williams, M. (2015). Constraining ecosystem carbon dynamics in a data-limited world: Integrating ecological “common sense” in a model-data fusion framework. *Biogeosciences*, 12(5), 1299–1315. <https://doi.org/10.5194/bg-12-1299-2015>
- Brooks, P. D., Williams, M. W., & Schmidt, S. K. (1998). Inorganic nitrogen and microbial biomass dynamics before and during spring snowmelt. *Biogeochemistry*, 43, 1–15.
- Chang, R. Y.-W., Miller, C. E., Dinardo, S. J., Karion, A., Sweeney, C., Daube, B. C., . . . Wofsy, S. C. (2014). Methane emissions from Alaska in 2012 from CARVE airborne observations. *Proceedings of the National Academy of Sciences*, 111(47), 16694–16699. <https://doi.org/10.1073/pnas.1412953111>
- Commane, R., Benmergui, J., Lindaas, J. O. W., Miller, S., Luus, K. A., Chang, R. Y.-W., . . . Wofsy, S. C. (2017). CARVE: Net ecosystem CO₂

- exchange and regional carbon budgets for Alaska, 2012–2014. Oak Ridge, TN: ORNL DAAC. <https://doi.org/10.3334/ORNLDAAC/1389>
- Commane, R., Lindaas, J., Benmergui, J., Luus, K. A., Chang, R. Y.-W., Daube, B. C., ... Wofsy, S. C. (2017). Carbon dioxide sources from Alaska driven by increasing early winter respiration from Arctic tundra. *Proceedings of the National Academy of Sciences of the United States of America*, 114(21), <https://doi.org/10.1073/pnas.1618567114>
- Cox, C. J., Stone, R. S., Douglas, D. C., Stanitski, D. M., Divoky, G. J., Dutton, G. S., ... Longenecker, D. U. (2017). Drivers and environmental responses to the changing annual snow cycle of northern Alaska. *Bulletin of the American Meteorological Society*, 98(12), 2559–2577.
- Davidson, S. J., Sloan, V. L., Phoenix, G. K., Wagner, R., Fisher, J. P., Oechel, W. C., & Zona, D. (2016). Vegetation type dominates the spatial variability in CH₄ emissions across multiple arctic tundra landscapes. *Ecosystems*, 19(6), 1116–1132. <https://doi.org/10.1007/s10021-016-9991-0>
- Demmig-Adams, B., & Adams, W. W. (1996). The role of xanthophyll cycle carotenoids in the protection of photosynthesis. *Trends in Plant Science*, 1, 21–26.
- Deng, F., Jones, D. B. A., O'Dell, C. W., Nassar, R., & Parazoo, N. C. (2016). Combining GOSAT XCO₂ observations over land and ocean to improve regional CO₂ flux estimates. *Journal of Geophysical Research – Atmospheres*, 121, 1896–1913. <https://doi.org/10.1002/2015JD024157>
- Elmendorf, S. C., Henry, G. H. R., Hollister, R. D., Björk, R. G., Boulanger-Lapointe, N., Cooper, E. J., ... Wipf, S. (2012). Plot-scale evidence of tundra vegetation change and links to recent summer warming. *Nature Climate Change*, 2(6), 453–457. <https://doi.org/10.1038/nclimate1465>
- Ensminger, I., Schmidt, L., & Lloyd, J. (2008). Soil temperature and intermittent frost modulate the rate of recovery of photosynthesis in Scots pine under simulated spring conditions. *New Phytologist*, 177, 428–442.
- Ensminger, I., Sveshnikov, D., Campbell, D. A., Funk, C., Jansson, S., Lloyd, J., ... Öquist, G. (2004). Intermittent low temperatures constrain spring recovery of photosynthesis in boreal Scots pine forests. *Global Change Biology*, 10(6), 995–1008. <https://doi.org/10.1111/j.1365-2486.2004.00781.x>
- Euskirchen, E. S., Bret-Harte, M. S., Shaver, G. R., Edgar, C. W., & Romanovsky, V. E. (2017). Long-term release of carbon dioxide from arctic tundra ecosystems in Alaska. *Ecosystems*, 20(5), 960–974. <https://doi.org/10.1007/s10021-016-0085-9>
- Euskirchen, E. S., Edgar, C. W., Turetsky, M. R., Waldrop, M. P., & Harden, J. W. (2014). Differential response of carbon fluxes to climate in three peatland ecosystems that vary in the presence and stability of permafrost. *Journal of Geophysical Research G: Biogeosciences*, 119(8), 1576–1595. <https://doi.org/10.1002/2014JG002683>
- Frankenberg, C., Fisher, J. B., Worden, J., Badgley, G., Saatchi, S. S., Lee, J. E., ... Yokota, T. (2011). New global observations of the terrestrial carbon cycle from GOSAT: Patterns of plant fluorescence with gross primary productivity. *Geophysical Research Letters*, 38(17), 1–22. <https://doi.org/10.1029/2011GL048738>
- Gonsamo, A., Chen, J. M., Price, D. T., Kurz, W. A., & Wu, C. (2012). Land surface phenology from optical satellite measurement and CO₂ eddy covariance technique. *Journal of Geophysical Research: Biogeosciences*, 117, G03032. <https://doi.org/10.1029/2012JG002070>
- Goodrich, J. P., Oechel, W. C., Gioli, B., Moreaux, V., Murphy, P. C., Burba, G., & Zona, D. (2016). Impact of different eddy covariance sensors, site set-up, and maintenance on the annual balance of CO₂ and CH₄ in the harsh Arctic environment. *Agricultural and Forest Meteorology*, 228–229, 239–251. <https://doi.org/10.1016/j.agrformet.2016.07.008>
- Goulden, M. L. (1998). Sensitivity of boreal forest carbon balance to soil thaw. *Science*, 279(5348), 214–217. <https://doi.org/10.1126/science.279.5348.214>
- Graven, H. D., Keeling, R. F., Piper, S. C., Patra, P. K., Stephens, B. B., Wofsy, S. C., ... Bent, J. D. (2013). Enhanced seasonal exchange of CO₂ by northern ecosystems since 1960. *Science (New York, N.Y.)*, 341(September), 1085–1089. <https://doi.org/10.1126/science.1239207>
- Griffis, T. J., Rouse, W. R., & Waddington, J. M. (2000). Interannual variability of net ecosystem CO₂ exchange at a subarctic fen. *Global Biogeochemical Cycles*, 14, 1109–1121.
- Guanter, L., Aben, I., Tol, P., Krijger, J. M., Hollstein, A., Köhler, P., & Landgraf, J. (2015). Potential of the TROPOspheric Monitoring Instrument (TROPOMI) onboard the Sentinel-5 Precursor for the monitoring of terrestrial chlorophyll fluorescence. *Atmospheric Measurement Techniques*, 8, 1337–1352.
- Harazono, Y., Mano, M., Miyata, A., Zulueta, R. C., & Oechel, W. C. (2003). Inter-annual carbon dioxide uptake at a wet sedge tundra ecosystem in the Arctic. *Tellus*, 55B, 215–231.
- Henderson, J. M., Eluszkiewicz, J., Mountain, M. E., Nehr Korn, T., Chang, R. Y. W., Karion, A., ... Miller, C. E. (2015). Atmospheric transport simulations in support of the Carbon in Arctic Reservoirs Vulnerability Experiment (CARVE). *Atmospheric Chemistry and Physics*, 15(8), 4093–4116. <https://doi.org/10.5194/acp-15-4093-2015>
- Hinzman, L. D., Deal, C. J., McGuire, A. D., Mernild, S. H., Polyakov, I. V., & Walsh, J. E. (2013). Trajectory of the Arctic as an integrated system. *Ecological Applications*, 23(8), 1837–1868. <https://doi.org/10.1890/11-1498.1>
- Hugelius, G., Strauss, J., Zubrzycki, S., Harden, J. W., Schuur, E. A. G., Ping, C.-L., & Kuhry, P. (2014). Estimated stocks of circumpolar permafrost carbon with quantified uncertainty ranges and identified data gaps. *Biogeosciences*, 11, 6573–6593.
- Ishida, A., Nakano, T., Sekikawa, S., Maruta, E., & Masuzawa, T. (2001). Diurnal changes in needle gas exchange in alpine *Pinus pumila* during snow-melting and summer seasons. *Ecological Research*, 16(1), 107–116.
- Jafarou, E., & Schaefer, K. (2016). The importance of a surface organic layer in simulating permafrost thermal and carbon dynamics. *Cryosphere*, 10(1), 465–475. <https://doi.org/10.5194/tc-10-465-2016>
- Jarvis, P., & Linder, S. (2000). Constraints to growth of boreal forests. *Nature*, 405(6789), 904–905. [https://doi.org/10.1002/\(SICI\)1097-0177\(199909\)216:1<1:AID-DVDY1>3.0.CO;2-T](https://doi.org/10.1002/(SICI)1097-0177(199909)216:1<1:AID-DVDY1>3.0.CO;2-T)
- Jeong, S., Medvigy, D., Shevliakova, E., & Malyshev, S. (2012). Uncertainties in terrestrial carbon budgets related to spring phenology. *Journal of Geophysical Research: Biogeosciences*, 117(March), 1–17. <https://doi.org/10.1029/2011JG001868>
- Jeong, S., Medvigy, D., Shevliakova, E., & Malyshev, S. (2013). Predicting changes in temperate forest budburst using continental-scale observations and models. *Geophysical Research Letters*, 40(2), 359–364. <https://doi.org/10.1029/2012gl054431>
- Jeong, S. J., Schimel, D., Frankenberg, C., Drewry, D. T., Fisher, J. B., Verma, M., ... Joiner, J. (2017). Application of satellite solar-induced chlorophyll fluorescence to understanding large-scale variations in vegetation phenology and function over northern high latitude forests. *Remote Sensing of Environment*, 190, 178–187. <https://doi.org/10.1016/j.rse.2016.11.021>
- Joiner, J., Yoshida, Y., Vasilkov, A. P., Middleton, E. M., Campbell, P. K. E., & Kuze, A. (2012). Filling-in of near-infrared solar lines by terrestrial fluorescence and other geophysical effects: Simulations and space-based observations from SCIAMACHY and GOSAT. *Atmospheric Measurement Techniques*, 5(4), 809.
- Joiner, J., Yoshida, Y., Vasilkov, A. P., Schaefer, K., & Jung, M. (2014). The seasonal cycle of satellite chlorophyll fluorescence observations and its relationship to vegetation phenology and ecosystem atmosphere carbon exchange. *Remote Sens. Environment*, 152, 375–391.
- Jonsson, A. M., Eklundh, L., Hellström, M., Barring, L., & Jönsson, P. (2010). Annual changes in MODIS vegetation indices of Swedish coniferous forests in relation to snow dynamics and tree phenology. *Remote Sensing of Environment*, 114, 2719–2730.

- Kim, Y., Kimball, J. S., Zhang, K., Didan, K., Velicogna, I., & McDonald, K. C. (2014). Attribution of divergent northern vegetation growth responses to lengthening non-frozen seasons using satellite optical-NIR and microwave remote sensing. *International Journal of Remote Sensing*, 35(10), 3700–3721. <https://doi.org/10.1080/01431161.2014.915595>
- Kim, Y., Kimball, J. S., Zhang, K., & McDonald, K. C. (2012). Satellite detection of increasing Northern Hemisphere non-frozen seasons from 1979 to 2008: Implications for regional vegetation growth. *Remote Sensing of Environment*, 121, 472–487. <https://doi.org/10.1016/j.rse.2012.02.014>
- Lafleur, P. M., & Humphreys, E. R. (2007). Spring warming and carbon dioxide exchange over low Arctic tundra in central Canada. *Global Change Biology*, 14, 740–756.
- Larsen, K. S., Grogan, P., Jonasson, S., & Michelsen, A. (2007). Respiration and microbial dynamics in two subarctic ecosystems during winter and spring thaw: effects of increased snow depth. *Arctic, Antarctic, and Alpine Research*, 39(2), 268–276.
- Lasslop, G., Reichstein, M., Papale, D., Richardson, A., Armeth, A., Barr, A., ... Wohlfahrt, G. (2010). Separation of net ecosystem exchange into assimilation and respiration using a light response curve approach: Critical issues and global evaluation. *Global Change Biology*, 16(1), 187–208. <https://doi.org/10.1111/j.1365-2486.2009.02041.x>
- Lawrence, D. M., & Slater, A. G. (2010). The contribution of snow condition trends to future ground climate. *Climate Dynamics*, 34(7), 969–981. <https://doi.org/10.1007/s00382-009-0537-4>
- Lawrence, D. M., Slater, A. G., Romanovsky, V. E., & Nicolsky, D. J. (2008). Sensitivity of a model projection of near-surface permafrost degradation to soil column depth and representation of soil organic matter. *Journal of Geophysical Research: Earth Surface*, 113(2), F02011. <https://doi.org/10.1029/2007JF000883>
- Liu, J., Bowman, K. W., Lee, M., Henze, D. K., Bousseres, N., Brix, H., ... Nassar, R. (2014). Carbon monitoring system flux estimation and attribution: Impact of ACOS-GOSAT XCO₂ sampling on the inference of terrestrial biospheric sources and sinks. *Tellus, Series B: Chemical and Physical Meteorology*, 66(1), 1–18. <https://doi.org/10.3402/telusb.v66.22486>
- Liu, J., Bowman, K. W., Schimel, D. S., Parazoo, N. C., Jiang, Z., Lee, M., ... Eldering, A. (2017). Contrasting carbon cycle responses of the tropical continents to the 2015–2016 El Niño. *Science*, 358(6360), <https://doi.org/10.1126/science.aam5690>
- Lokupitiya, R. S., Zupanski, D., Denning, A. S., Kawa, S. R., Gurney, K. R., & Zupanski, M. (2008). Estimation of global CO₂ fluxes at regional scale using the maximum likelihood ensemble filter. *Journal of Geophysical Research*, 113, D20110. <https://doi.org/10.1029/2007JD009679>
- Luus, K. A., Commane, R., Parazoo, N. C., Benmergui, J., Euskirchen, E. S., Frankenberg, C., ... Zona, D. (2017). Tundra photosynthesis captured by satellite-observed solar-induced chlorophyll fluorescence. *Geophysical Research Letters*, 44(3), 1564–1573.
- Luus, K. A., & Lin, J. C. (2015). The polar vegetation photosynthesis and respiration model: A parsimonious, satellite-data-driven model of high-latitude CO₂ exchange. *Geoscientific Model Development*, 8(8), 2655–2674. <https://doi.org/10.5194/gmd-8-2655-2015>
- McGuire, A. D., Christensen, T. R., Hayes, D., Heroult, A., Euskirchen, E., Kimball, J. S., ... Yi, Y. (2012). An assessment of the carbon balance of Arctic tundra: Comparisons among observations, process models, and atmospheric inversions. *Biogeosciences*, 9(8), 3185–3204. <https://doi.org/10.5194/bg-9-3185-2012>
- Messerschmidt, J., Parazoo, N., Wunch, D., Deutscher, N. M., Roehl, C., Warneke, T., & Wennberg, P. O. (2013). Evaluation of seasonal atmosphere-biosphere exchange estimations with TCCON measurements. *Atmospheric Chemistry and Physics*, 13(10), 5103–5115.
- Müller, P., Li, X. P., & Niyogi, K. K. (2001). Non-photochemical quenching. A response to excess light energy. *Plant Physiology*, 125, 1558–1566.
- Natali, S. M., Schuur, E. A. G., & Rubin, R. L. (2012). Increased plant productivity in Alaskan tundra as a result of experimental warming of soil and permafrost. *Journal of Ecology*, 100(2), 488–498. <https://doi.org/10.1111/j.1365-2745.2011.01925.x>
- Oberbaur, S. F., Starr, G., & Pop, E. W. (1998). Effects of extended growing season and soil warming on carbon dioxide and methane exchange of tussock tundra in Alaska. *Journal of Geophysical Research: Atmospheres*, 103, 29075–29082.
- Ott, L. E., Pawson, S., Collatz, G. J., Gregg, W. W., Menemenlis, D., Brix, H., ... Gunson, M. R. (2015). Assessing the magnitude of CO₂ flux uncertainty in atmospheric CO₂ records using products from NASA's Carbon Monitoring Flux Pilot Project. *Journal of Geophysical Research: Atmospheres*, 120(2), 734–765.
- Ottander, C., Campbell, D., & Oquist, G. (1995). Seasonal changes in photosystem II organization and pigment composition in *Pinus sylvestris*. *Planta*, 197, 176–183.
- Parazoo, N. C., Bowman, K., Fisher, J. B., Frankenberg, C., Jones, D. B., Cescatti, A., ... Montagnani, L. (2014). Terrestrial gross primary production inferred from satellite fluorescence and vegetation models. *Global Change Biology*, 20, 3103–3121.
- Parazoo, N. C., Commane, R., Wofsy, S. C., Koven, C. D., Sweeney, C., Lawrence, D. M., & Miller, C. E. (2016). Detecting regional patterns of changing CO₂ flux in Alaska. *Proceedings of the National Academy of Sciences of the United States of America*, 113(28), <https://doi.org/10.1073/pnas.1601085113>
- Parazoo, N. C., Denning, A. S., Kawa, S. R., Pawson, S., & Lokupitiya, R. (2012). CO₂ flux estimation errors associated with moist atmospheric processes. *Atmospheric Chemistry and Physics*, 12, 6405–6416.
- Peng, S., Ciais, P., Chevallier, F., Peylin, P., Cadule, P., Sitch, S., ... Zhao, H. (2015). Benchmarking the seasonal cycle of CO₂ fluxes simulated by terrestrial ecosystem models. *Global Biogeochemical Cycles*, 29, 46–64. <https://doi.org/10.1002/2014GB004931>
- Peters, W., Jacobson, A. R., Sweeney, C., Andrews, A. E., Conway, T. J., Masarie, K., ... Tans, P. P. (2007). An atmospheric perspective on North American carbon dioxide exchange: CarbonTracker. *Proceedings of the National Academy of Sciences*, 104, 18925–18930.
- Porcar-Castell, A. (2011). A high-resolution portrait of the annual dynamics of photochemical and non-photochemical quenching in needles of *Pinus sylvestris*. *Physiologia Plantarum*, 143, 139–153.
- Potter, C., Klooster, S., & Genovese, V. (2013). Alaska ecosystem carbon fluxes estimated from MODIS satellite data inputs from 2000 to 2010. *Carbon Balance and Management*, 8(1), 12.
- Pulliainen, J., Aurela, M., Laurila, T., Aalto, T., Takala, M., Salminen, M., ... Laaksonen, A. (2017). Early snowmelt significantly enhances boreal springtime carbon uptake. *Proceedings of the National Academy of Sciences*, 114(42), 11081–11086.
- Ramage, J. M., & Isacks, B. L. (2002). Determination of melt-onset and refreeze timing on southeast Alaskan icefields using SSM/I diurnal amplitude variations. *Annals of Glaciology*, 34, 391–398.
- Reichstein, M., Falge, E., Baldocchi, D., Papale, D., Aubinet, M., Berbigier, P., ... Valentini, R. (2005). On the separation of net ecosystem exchange into assimilation and ecosystem respiration: Review and improved algorithm. *Global Change Biology*, 11(9), 1424–1439. <https://doi.org/10.1111/j.1365-2486.2005.001002.x>
- Richardson, A. D., Braswell, B. H., Hollinger, D. Y., Jenkins, J. P., & Ollinger, S. V. (2011). Near-surface remote sensing of spatial and temporal variation in canopy phenology. *Ecological Applications*, 19, 1417–1428.
- Romanovsky, V. E., & Osterkamp, T. E. (2000). Effects of unfrozen water on heat and mass transport processes in the active layer and permafrost. *Permafrost and Periglacial Processes*, 11(3), 219–239.
- Rödenbeck, C. (2005). Estimating CO₂ sources and sinks from atmospheric mixing ratio measurements using a global inversion of atmospheric transport, Technical Report 6, Max Planck Institute for Biogeochemistry, Jena.

- Rödenbeck, C., Houweling, S., Gloor, M., & Heimann, M. (2003). CO₂ flux history 1982–2001 inferred from atmospheric data using a global inversion of atmospheric transport. *Atmospheric Chemistry and Physics*, 3, 1919–1964.
- Schaefer, K., Schwalm, C. R., Williams, C., Arain, M. A., Barr, A., Chen, J. M., ... Zhou, X. (2012). A model-data comparison of gross primary productivity: Results from the north American carbon program site synthesis. *Journal of Geophysical Research: Biogeosciences*, 117(3), 1–15. <https://doi.org/10.1029/2012JG001960>
- Soukupova, J., Csefalvay, L., Urban, O., Kosvancova, M., Marek, M., Rascher, U., & Nedbal, L. (2008). Annual variation of the steady-state chlorophyll fluorescence emission of evergreen plants in temperate zone. *Functional Plant Biology*, 35, 63–76.
- Springer, K. R., Wang, R., & Gamon, J. A. (2017). Parallel seasonal patterns of photosynthesis, fluorescence, and reflectance indices in boreal trees. *Remote Sensing*, 9, 691. <https://doi.org/10.3390/rs9070691>
- Starr, G., & Oberbauer, S. (2003). Photosynthesis of arctic evergreens under snow: implications for tundra ecosystem carbon balance. *Ecology*, 84, 1415–1420.
- Steiner, N., McDonald, K. C., Dinardo, S. J., & Miller, C. E. (2015). Snowmelt and Surface Freeze/Thaw Timings over Alaska derived from Passive Microwave Observations using a Wavelet Classifier, AGU Fall Meeting Abstracts
- Steiner, N., McDonald, K. C., & Miller, C. E. (2017a). Snowmelt and Freeze/Thaw Mapping of Boreal and Arctic Alaska using Wavelet Analysis. IEEE Transactions on Geoscience and Remote Sensing, In-Prep.
- Steiner, N., McDonald, K. C., & Miller, C. E. (2017b). CARVE: Daily Thaw State of Boreal and Arctic Alaska from AMSR-E and SSM/I, 2003–2014. Oak Ridge, TN: ORNL DAAC. <https://doi.org/10.3334/ornl/daac/1383>
- Steiner, N., & Tedesco, M. (2014). A wavelet melt detection algorithm applied to enhanced-resolution scatterometer data over Antarctica (2000–2009). *The Cryosphere*, 8(1), 25. <https://doi.org/10.5194/tc-8-25-2014>
- Strand, M., & Öquist, G. (1985). Inhibition of photosynthesis by freezing temperatures and high light levels in cold-acclimated seedlings of Scots pine (*Pinus sylvestris*): I. Effects on the light-limited and light-saturated rates of CO₂ assimilation. *Physiologia Plantarum*, 64, 425–430. <https://doi.org/10.1111/j.1399-3054.1985.tb08517.x>
- Sun, Y., Frankenberg, C., Jung, M., Joiner, J., Guanter, L., Köhler, P., & Magney, T. (2018). Overview of solar-induced fluorescence (SIF) from the Orbiting Carbon Observatory-2: Retrieval, cross-mission comparison, and global monitoring for GPP. *Remote Sensing of Environment*, 209, 808–823. <https://doi.org/10.1016/j.rse.2018.02.016>
- Tanja, S., Berninger, F., Vesala, T., Markkanen, T., Hari, P., & Makela, A. (2003). Air temperature triggers the recovery of evergreen boreal forest photosynthesis in spring. *Global Change Biology*, 9, 1410–1426.
- Troeng, E., & Linder, S. (1982). Gas exchange in a 20-year-old stand of Scots pine. I. Net photosynthesis of current and one-year-old shoots within and between seasons. *Physiologia Plantarum*, 54, 7–14.
- Ueyama, M., Iwata, H., Harazono, Y., Euskirchen, E. S., Oechel, W. C., & Zona, D. (2013). Growing season and spatial variations of carbon fluxes of Arctic and boreal ecosystems in Alaska (USA). *Ecological Applications*, 23, 1798–1816.
- Van der Werf, G. R., Randerson, J. T., Giglio, L., Collatz, G. J., Mu, M., Kasibhatla, P. S., ... van Leeuwen, T. T. (2010). Global fire emissions and the contribution of deforestation, savanna, forest, agricultural, and peat fires (1997–2009). *Atmospheric Chemistry and Physics*, 10(23), 11707–11735.
- Walther, S., Voigt, M., Thum, T., Gonsamo, A., Zhang, Y., Köhler, P., ... Guanter, L. (2016). Satellite chlorophyll fluorescence measurements reveal large-scale decoupling of photosynthesis and greenness dynamics in boreal evergreen forests. *Global Change Biology*, 22(9), 2979–2996. <https://doi.org/10.1111/gcb.13200>
- Wang, T., Brender, P., Ciais, P., Piao, S., Mahecha, M. D., Chevallier, F., ... Vacarri, F. P. (2012). State-dependent errors in a land surface model across biomes inferred from eddy covariance observations on multiple timescales. *Ecological Modelling*, 246, 11–25.
- Waring, R. H., & Winner, W. E. (1996). Constraints on terrestrial primary production along the Pacific Coast of North and South America. In R. G. Lawford, P. Alaback, & E. R. Fuentes (Eds.), *High latitude rain forests and associated ecosystems of the west coast of the Americas: Climate, hydrology, ecology, and conservation* (pp. 89–102). New York, NY: Springer-Verlag.
- Wolfe, G. M., Kawa, S. R., Hanisco, T. F., Hannun, R. A., Newman, P. A., Swanson, A., ... DiGangi, J. (2018). The NASA Carbon Airborne Flux Experiment (CARAFE): Instrumentation and methodology. *Atmospheric Measurement Techniques*, 11(3), 1757.
- Wong, C. Y. S., & Gamon, J. A. (2015). The photochemical reflectance index provides an optical indicator of spring photosynthetic activation in evergreen conifers. *New Phytologist*, 206(1), 196–208. <https://doi.org/10.1111/nph.13251>
- Yi, S., Wischnewski, K., Langer, M., Muster, S., & Boike, J. (2014). Freeze/thaw processes in complex permafrost landscapes of northern Siberia simulated using the TEM ecosystem model: Impact of thermokarst ponds and lakes. *Geoscientific Model Development*, 7(4), 1671–1689. <https://doi.org/10.5194/gmd-7-1671-2014>
- Zhang, K., Kimball, J. S., Kim, Y., & McDonald, K. C. (2011). Changing freeze-thaw seasons in northern high latitudes and associated influences on evapotranspiration. *Hydrological Processes*, 25(26), 4142–4151. <https://doi.org/10.1002/hyp.8350>
- Zona, D., Beniamigo, G., Commane, R., Lindaas, J., Wofsy, S. C., Miller, C. E., & Oechel, W. C. (2016). Cold season emissions dominate the Arctic tundra methane budget. *Proceedings of the National Academy of Sciences*, 133(1), 40–45.
- Zona, D., Oechel, W. C., Richards, J. H., Hastings, S., Kopetz, I., Ikawa, H., & Oberbauer, S. (2011). Light-stress avoidance mechanisms in a Sphagnum-dominated wet coastal Arctic tundra ecosystem in Alaska. *Ecology*, 92(3), 633–644. <https://doi.org/10.1890/10-0822.1>

SUPPORTING INFORMATION

Additional supporting information may be found online in the Supporting Information section at the end of the article.

How to cite this article: Parazoo NC, Arneith A, Pugh TAM, et al. Spring photosynthetic onset and net CO₂ uptake in Alaska triggered by landscape thawing. *Glob Change Biol*. 2018;24:3416–3435. <https://doi.org/10.1111/gcb.14283>